Research Square

Preprints are preliminary reports that have not undergone peer review.
They should not be considered conclusive, used to inform clinical practice,
or referenced by the media as validated information.

A Progressive Damage Model for Predicting Tensile Performance of Composite Single-Bolt Double-Shear Joints with Prefabricated Hole-Edge Delamination: Unveiling Size-Dependent Delamination Behavior

Y. M. Li
Nanjing University of Aeronautics and Astronautics
Z. R. Wu
zrwu@nuaa.edu.cn

Nanjing University of Aeronautics and Astronautics
H. Lei
AVIC Chengdu Aircraft Design and Research Institute
W. Y. Yuan
Nanjing University of Aeronautics and Astronautics
S. Z. Ma
Nanjing University of Aeronautics and Astronautics
M. L. Chen
Nanjing University of Aeronautics and Astronautics

Research Article

Keywords: Composite materials, Single-bolt double-shear joint, Hole-edge delamination, Progressive damage analysis, Cohesive zone model

Posted Date: August 24th, 2026

DOI: https://doi.org/10.21203/rs.3.rs-10524938/v1

License: This work is licensed under a Creative Commons Attribution 4.0 International License.
Read Full License

Additional Declarations: No competing interests reported.

A Progressive Damage Model for Predicting Tensile Performance of Composite Single-Bolt Double-Shear Joints with Prefabricated Hole-Edge Delamination: Unveiling Size-Dependent Delamination Behavior

Y.M. Li[a*], Z.R. Wu[a*], H. Lei[b], W.Y. Yuan[a], S.Z. Ma[a], M.L. Chen[a]

College of Energy and Power Engineering, Nanjing University of Aeronautics and Astronautics, Nanjing 210016, China

[b]AVIC Chengdu Aircraft Design and Research Institute, Chengdu 610041, China

"[a*]": These authors contributed equally to this work.

Corresponding author: Z.R. Wu

E-mail: zrwu@nuaa.edu.cn

Address: College of Energy and Power Engineering, Nanjing University of Aeronautics and Astronautics, Nanjing, Jiangsu 210016, China

Abstract: Composite single-bolt double-shear joints with prefabricated hole-edge delamination are systematically investigated through experimental and numerical approaches. Tensile tests are conducted on specimens with delamination diameters of 0, 12, 20 and 28 mm. A three-dimensional progressive damage model incorporating the Hashin-type failure criterion and Camanho degradation model is developed using a UMAT subroutine, with cohesive elements introduced to simulate delamination. Numerical predictions agree well with experiments, with errors within 10%. Parametric studies reveal that delamination location, shape, and orientation all significantly affect joint performance. Small delaminations propagate extensively beyond their initial region, whereas large delaminations exhibit limited propagation beyond the prefabricated defect. The ultimate load decreases by 5.7% as the delamination diameter increases from 0 to 28 mm. The proposed method provides a reliable tool for damage-tolerant design of composite bolted joints.

Keyword: Composite materials; Single-bolt double-shear joint; Hole-edge delamination; Progressive damage analysis; Cohesive zone model

1. Introduction

Advanced composite materials have been extensively applied in the aerospace industry due to their outstanding properties, including high specific strength, high specific stiffness, excellent fatigue resistance, and design flexibility [1-4]. In commercial aviation, the Boeing 787 and Airbus A350 feature composite content exceeding 50% of their structural weight, while the domestically developed C919 also incorporates substantial proportions of composites in its primary structures [5,6]. This trend reflects the growing reliance on composites for weight reduction, fuel efficiency, and enhanced structural performance in modern aircraft [7,8].

Despite the inherent designability of composite materials, mechanical joints remain indispensable in composite structures due to considerations of manufacturing, assembly, and maintenance [9,10]. Bolted joints are widely employed in composite structures owing to their reliability, load-transfer capability, and disassembly characteristics [11]. However, the drilling

process required for bolted joints introduces stress concentrations and potential defects around the hole, which significantly affect the structural integrity and load-bearing capacity of the joint [12,13]. Recent studies have also highlighted the influence of manufacturing-induced defects on the long-term durability of composite joints under various loading conditions [14,15].

Substantial efforts have been devoted to understanding the failure mechanisms and load-bearing capacity of composite bolted joints. Camanho and Matthews [16] developed a foundational progressive damage model for mechanically fastened joints, identifying the interaction between bearing damage and delamination as a critical factor governing joint strength. Building on this framework, recent investigations have extended to hybrid joining techniques and complex joint configurations. Zhang et al. [17] employed acoustic emission monitoring combined with clustering algorithms to characterise damage evolution in hybrid bonded-bolted composite joints, revealing the sequential load-transfer mechanism between the adhesive layer and bolts. Kumar et al. [18] investigated the effect of bolt preload on the fatigue behaviour of composite single-lap joints, demonstrating that moderate preload significantly improves fatigue life by suppressing fretting and delamination. The influence of geometric parameters on joint performance has also been examined [19,20]. Wang et al. [21] conducted a comprehensive parametric study on the bearing strength of composite bolted joints, identifying the coupled effects of hole clearance and stacking sequence on failure progression.

Delamination is one of the most critical damage modes in composite laminates, accounting for more than 50% of manufacturing-induced defects [22]. The initiation and propagation of delamination are governed by interlaminar stresses arising from mismatched ply orientations and thickness direction stress components [23,24]. In composite bolted joints, delamination typically involves mixed-mode failure, with mode I initiated by axial bolt action and mode II induced by bearing stress between the bolt and hole wall [25]. Recent studies have demonstrated that delamination propagation paths are strongly influenced by the stacking sequence and the resulting interlaminar stress distributions [26,27]. Zhang et al. [28] investigated the effect of ply orientation on delamination resistance in composite laminates under mixed-mode loading, providing quantitative guidelines for optimising stacking sequences to enhance delamination tolerance. The presence of hole-edge delamination, in particular, has been identified as a critical factor that can reduce the bearing capacity of bolted joints significantly [29].

Numerical methods for delamination simulation have been extensively developed, including the virtual crack closure technique (VCCT), the extended finite element method (XFEM), and the cohesive zone model (CZM) [30]. The CZM has gained widespread acceptance because it does not require pre-existing cracks to predict delamination initiation and can simultaneously simulate both initiation and propagation [31,32]. Bilinear traction-separation laws are commonly employed with the CZM due to their balance of computational efficiency and accuracy [33]. The application of cohesive elements to delamination problems in composite joints has been explored by several researchers [34,35]. Three-dimensional Hashin-type failure criteria have also been widely adopted for predicting intralaminar damage in composite structures [36,37]. More

recently, machine learning approaches have emerged as a promising tool for accelerating delamination prediction in composite joints, though these methods typically require extensive training data and lack the physical interpretability of traditional models [38,39].

In the context of composite joints, delamination defects are commonly generated around bolt holes during the drilling process due to cutting-induced axial forces [40,41]. Ho-Cheng and Dharan [42] established a critical thrust force model for delamination during drilling, based on the energy balance between delamination fracture energy and work done by the thrust force. Jain and Yang [43] refined this model by incorporating the anisotropic properties of the laminate. However, several gaps remain in the existing body of knowledge. First, systematic investigation of prefabricated hole-edge delamination in single-bolt double-shear composite joints remains scarce, with most studies focusing on delamination in plain laminates rather than in joint configurations. Second, the effects of delamination shape and orientation on joint performance have rarely been reported; existing studies typically assume circular delamination shapes, whereas actual defects may exhibit various geometries due to inherent variability in the drilling process. Third, although three-dimensional Hashin-type criteria and cohesive zone models have been well established, their application to bolted joints with prefabricated delamination lacks systematic experimental validation across multiple parameters [44,45].

To address these gaps, this study conducts a systematic experimental and numerical investigation on the tensile performance of composite single-bolt double-shear joints with prefabricated hole-edge delamination. A series of tensile tests is performed on specimens with four delamination diameters (0, 12, 20 and 28 mm). A three-dimensional progressive damage model incorporating the Hashin-type failure criterion, the Camanho degradation model, and a cohesive zone model is developed and implemented via a UMAT subroutine in ABAQUS. The numerical model is validated against experimental results in terms of ultimate loads, load-displacement curves, failure modes, and delamination propagation patterns. Parametric studies are then conducted to systematically examine the effects of delamination location, shape, and orientation on joint damage and failure. This work provides a validated numerical tool and practical guidelines for the damage-tolerant design of composite bolted joints in aerospace applications.

The overall research framework of this study is illustrated in Fig. 1.1. The study comprises three main parts: experimental investigation, finite element modeling, and numerical analysis. In Chapter 2, tensile tests are conducted to obtain benchmark data. In Chapter 3, a progressive damage finite element model is developed and validated against the experimental results. In Chapter 4, parametric studies are performed based on the validated model to investigate the effects of delamination parameters on joint performance.

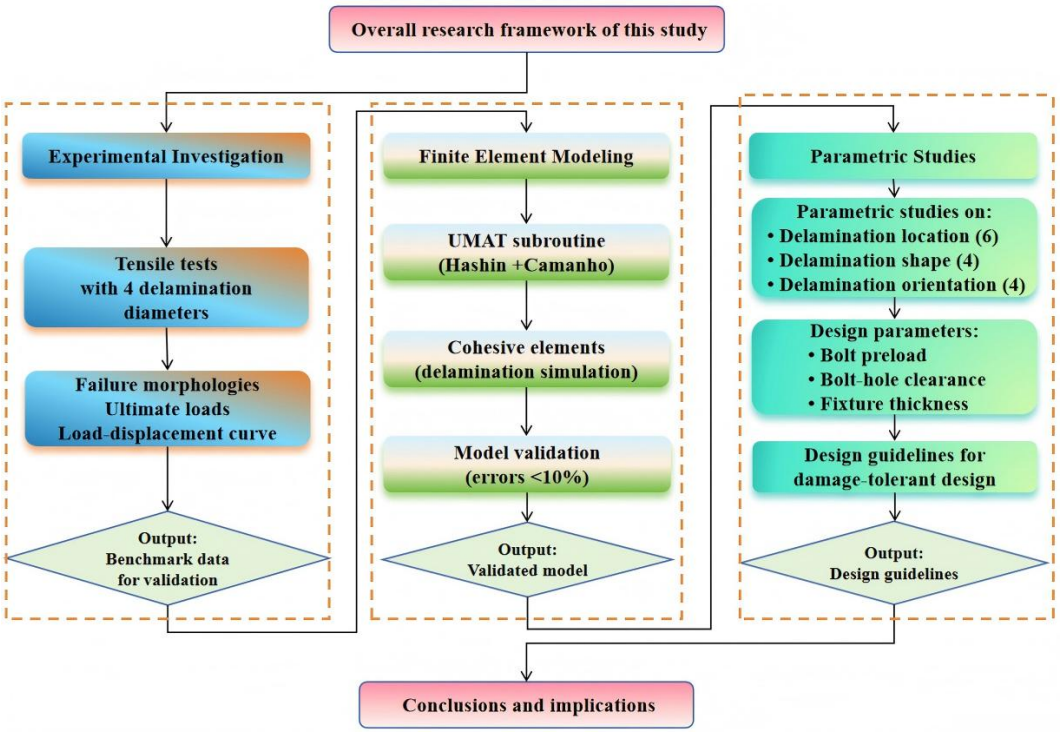


Fig. 1.1 Overall research framework of this study

2.Experimental Investigation

2.1 Specimen Fabrication

In this chapter, tensile static tests are conducted on composite single-bolt double-shear joints with prefabricated hole-edge delamination to systematically investigate the effect of delamination diameter on the mechanical performance of the joint structure. The experimental procedure is illustrated in Fig. 2.1, which consists of three main parts: specimen design, test setup and loading protocol, and experimental results and analysis.

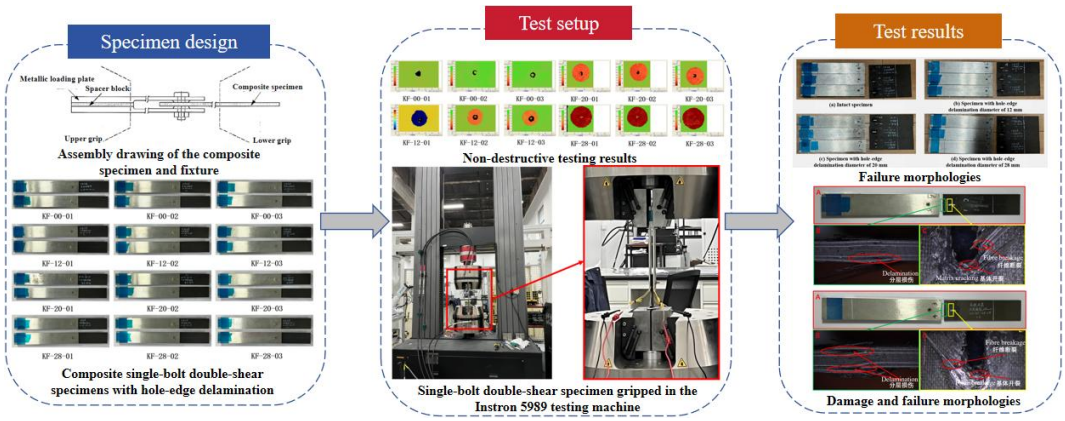
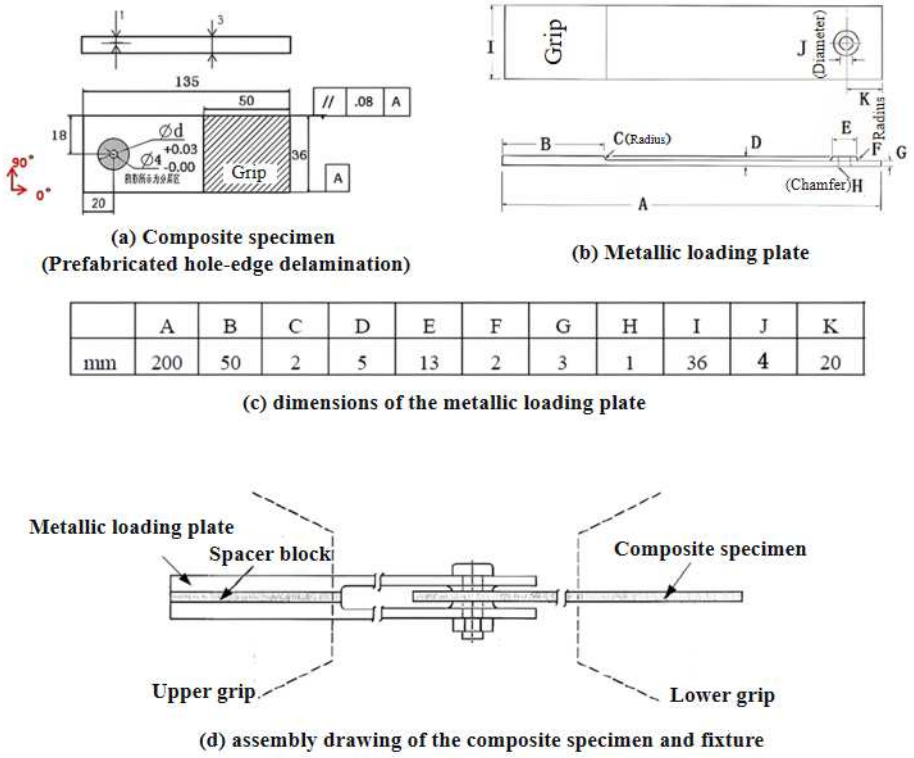


Figure 2.1 Flowchart of the experimental procedure

The specimens used in this study were single-bolt double-shear (SBDS) joint specimens fabricated in accordance with ASTM D5961. Each specimen assembly consisted of three primary components: a composite laminate, metallic fixture components, and a bolt assembly, as illustrated in Fig. 2.2.



(a) Composite specimen (Prefabricated hole-edge delamination)

(b) Metallic loading plate

	A	B	C	D	E	F	G	H	I	J	K
mm	200	50	2	5	13	2	3	1	36	4	20

(c) dimensions of the metallic loading plate

(d) assembly drawing of the composite specimen and fixture

Figure 2.2 Schematic diagram of the composite single-bolt double-shear joint with hole-edge delamination

The composite laminate was manufactured from ZT7H3194U/QY9512 carbon fiber/epoxy prepreg with a resin weight content of 33 ± 2%. The laminate had nominal dimensions of 135 mm (length) × 36 mm (width) × 3 mm (thickness), and consisted of 24 plies with a nominal cured ply thickness of 0.125 mm. The stacking sequence was [45/-45/90/-45/0/45/90/-45/45/0/-45/45]s, with ply proportions of 66% ±45°, 17% 0°, and 17% 90°, as detailed in Table 2.1.

Table 2.1Ply layup of the composite laminate

Plydesignation	Stackingsequence	Plyproportion（%）	Numberofplies	Thickness
A	[45/-45/90/-45/0/45/90/-45/45/0/-45/45]s	66/17/17	24	3

To investigate the effect of hole-edge delamination on the mechanical performance of the joint structure, prefabricated circular delamination was introduced at one-third of the laminate thickness, that is, between the 8th and 9th plies, by inserting a thin film during the layup process. The delamination region was located at the hole edge, as indicated by the shaded area in Fig. 2.2(a). Four delamination diameters were considered: 0 mm (intact), 12 mm, 20 mm, and 28 mm.

The metallic fixture assembly consisted of two loading plates and one spacer block, as shown in Fig. 2.2(b) and (c), all made of 30CrMnSiA steel and subjected to heat treatment, zinc plating (12–18 μm), passivation, and hydrogen removal. The bolt assembly comprised a bolt (HB7432F-4-24), a nut (HB8248MJ4×0.7), and a washer (HB1-521LB 4×10×1.5). A tightening torque of 3.4 N·m was applied to the bolt, and threads were not permitted to enter the joint region. The overall

assembly is shown in Fig. 2.2(d), where the laminate and fixture were tightly connected by the bolt, with the fixture arranged in a two-plate-one-block configuration.

A total of 16 specimens were fabricated, with four specimens for each delamination diameter (three for formal testing and one as a spare). The specimen designation system is presented in Fig. 2.3, and a complete list of specimen configurations is provided in Table 2.2. Photographs of the fabricated specimens are shown in Fig. 2.4.

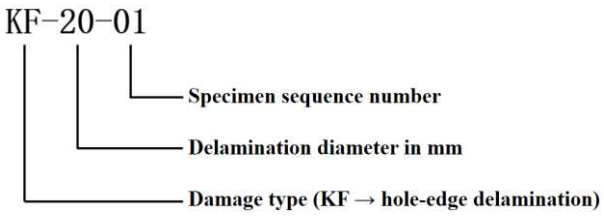


Figure2.3 Specimen designation system

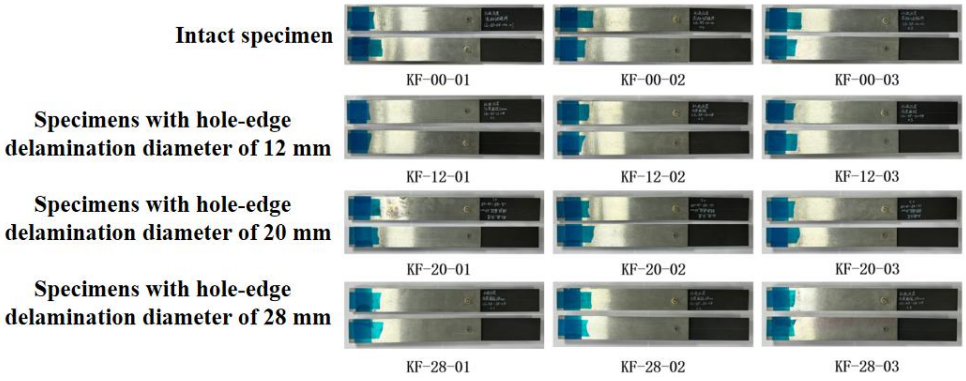


Figure 2.4 Front and back views of the composite single-bolt double-shear specimens with hole-edge delamination

Table 2.2Component list of the composite single-bolt double-shear specimens with hole-edge delamination

Specimentype	Specimendesignation	Component	Quantityperspecimen	Numberofspecimens
Delamination diameter of 0 mm (intact specimen)	KF-00-01:04	Intact composite specimen	1	4
		Metallic loading plate	2	
		Spacer block	1	
		Bolt: HB7432F-4-24	1	
		Nut: HB8248MJ4×0.7	1	
		Washer: HB8248MJ4×0.7	1	
Delamination diameter of 12 mm	KF-12-01:04	Composite specimen with 12 mm delamination diameter	1	4
		Metallic loading plate	2	
		Spacer block	1	
		Nut: HB7432F-4-24	1	
		Washer: HB8248MJ4×0.7	1	
		Washer: HB1-521LB 4×10×1.5	1	
Delamination diameter of 20 mm	KF-20-01:04	Composite specimen with 20 mm delamination diameter	1	4
		Metallic loading plate	2	
		Spacer block	1	
		Bolt: HB7432F-4-24	1	
		Nut: HB8248MJ4×0.7	1	
		Washer: HB1-521LB 4×10×1.5	1	
Delamination diameter of 28 mm	KF-28-01:04	Composite specimen with 28 mm delamination diameter	1	4
		Metallic loading plate	2	
		Spacer block	1	
		Bolt: HB7432F-4-24	1	
		Nut: HB8248MJ4×0.7	1	
		Washer: HB1-521LB 4×10×1.5	1	

2.2 Test Setup and Procedure

2.2.1 Pre-test Preparation

Prior to formal testing, all equipment including the testing machine, strain gauges, strain indicators, and data acquisition software were inspected to ensure that the entire testing system satisfied the required loading and measurement accuracy. All sensors, instruments, and gauges had been calibrated and were within their valid certification periods.

All 12 specimens were examined using ultrasonic C-scan technique, and the results are presented in Fig. 2.5. For the intact specimens (delamination diameter of 0 mm), only the bolt hole region exhibited indications, while the remaining areas were free of defects. For the three groups of specimens with prefabricated delamination, distinct defect regions were observed around the bolt hole, and the damaged area increased progressively with increasing delamination diameter. These results confirmed that the fabricated specimens were free from unintended defects and were suitable for formal tensile testing.

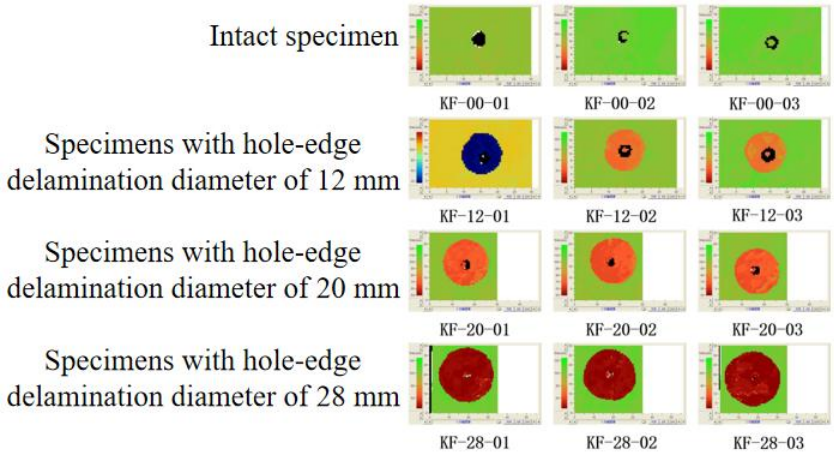


Figure 2.5 Non-destructive testing results of the composite single-bolt double-shear specimens with hole-edge delamination

2.2.2 Test Setup and Loading Protocol

Static tension tests were conducted using an Instron 5989 electro-hydraulic servo testing machine, as shown in Fig. 2.6. The machine had a load capacity of ±600 kN with a measurement accuracy of 0.5% of the indicated value, and a displacement range of 2000 mm with an accuracy of 0.05% of the indicated value. During testing, the metallic fixture end of the specimen was gripped by the upper wedge of the testing machine, while the composite laminate end was gripped by the lower wedge. Care was taken during installation to ensure that the specimen was vertically aligned and firmly seated against both grips. Strain gauges of type BX350-3AA (resistance 350 Ω ± 0.2) were pre-attached to the specimens, and a LAS-400 strain indicator was used in conjunction with the testing machine.

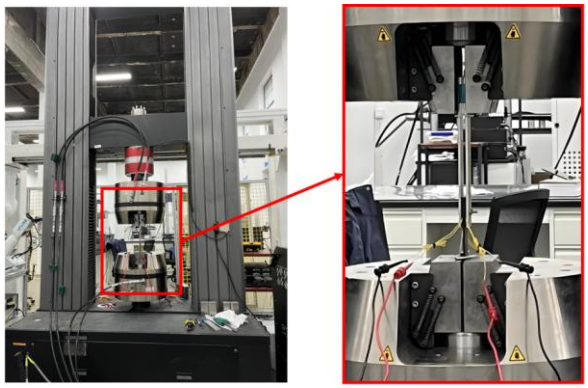


Figure 2.6 Single-bolt double-shear specimen gripped in the Instron 5989 testing machine

Displacement-controlled loading was applied at a crosshead speed of 1 mm/min. Load and displacement data were recorded in real time throughout each test to generate load-displacement curves. The tests were conducted in accordance with ASTM D5961, and loading continued until specimen failure was observed. All tests were performed under RTD (Room Temperature Dry) conditions, that is, at 21 ± 5.5°C with moisture content in the as-manufactured state.

2.3 Experimental Results and Analysis

2.3.1 Failure Mechanism Analysis

Post-test photographs of the four types of specimens are presented in Fig. 2.7. All specimens exhibited significant failure, with damage predominantly concentrated around the bolt hole of the laminate.

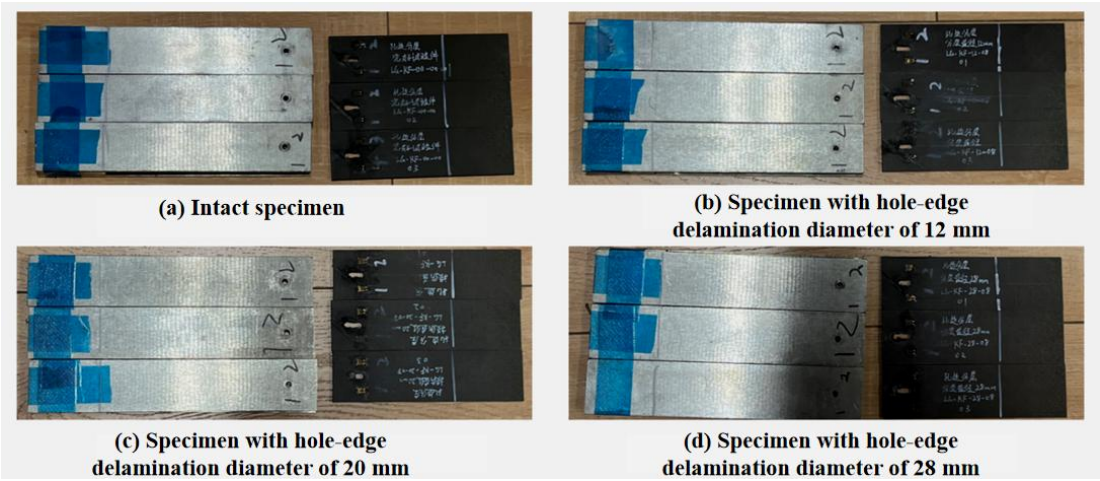
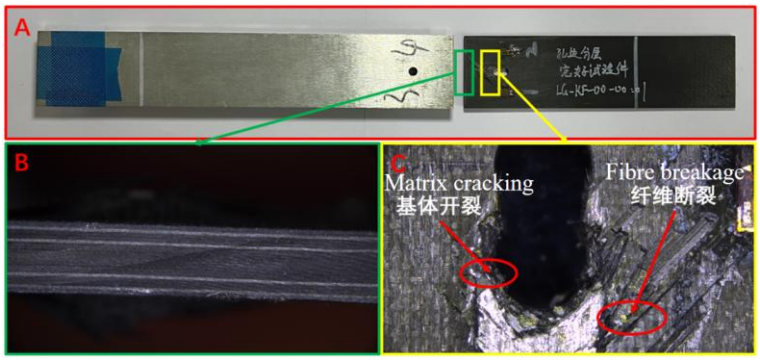
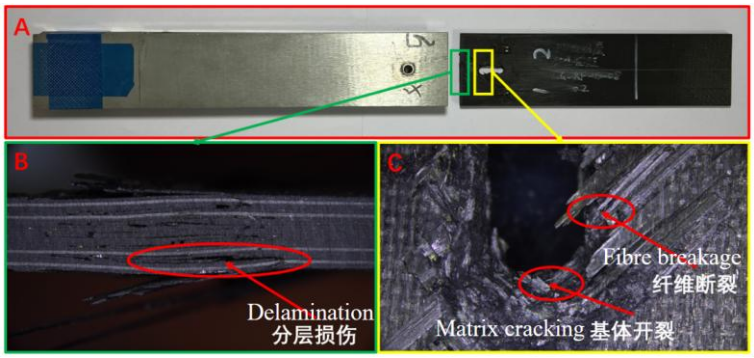


Figure 2.7 Failure morphologies of four types of composite single-bolt double-shear specimens with hole-edge delamination

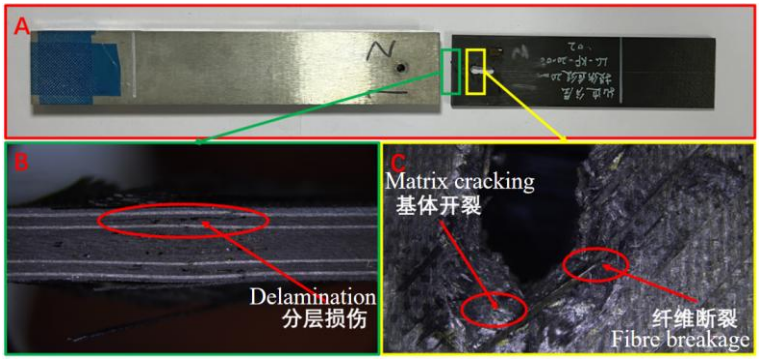
To further investigate the damage characteristics, optical microscopy was employed to examine the microscopic damage morphologies of each specimen type, as shown in Fig. 2.8, where Fig. A shows the overall failure morphology, and Figs. B and C are micrographs taken under high magnification. Since the damage morphologies of specimens within the same type were essentially consistent, one representative specimen from each type was selected for detailed analysis.



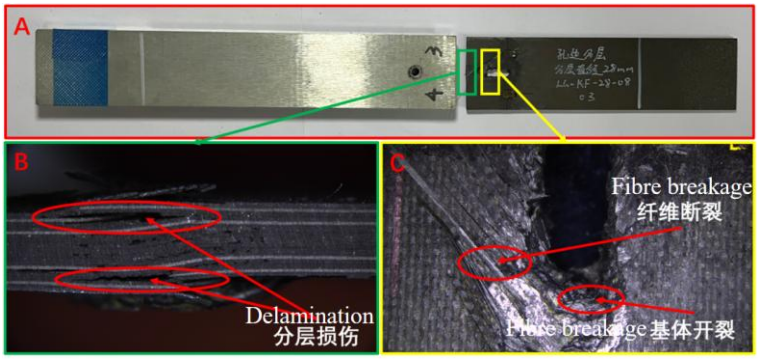
(a) Failure morphology of the intact specimen



(b) Failure morphology of the specimen with hole-edge delamination diameter of 12 mm



(c) Failure morphology of the specimen with hole-edge delamination diameter of 20 mm



(d) Failure morphology of the specimen with hole-edge delamination diameter of 28 mm

Figure 2.8 Damage and failure morphologies of four types of composite single-bolt double-shear specimens with hole-edge delamination

From the macroscopic failure morphologies, all four groups exhibited severe failure under tensile loading, with damage concentrated around the hole periphery, primarily characterized by bearing failure. On the compression side of the hole,

significant bearing deformation was observed, and fiber bundles separated from the laminate surface along the 45° direction, which is attributed to fiber buckling and fiber/matrix debonding caused by stress concentration at the hole edge.

From the microscopic failure morphologies, Fig. B presents the side view of the laminate on the compression side. The intact specimen showed no delamination on the side face, while all three groups with prefabricated delamination exhibited delamination to varying degrees. The intact specimen, free from prefabricated defects, maintained better structural integrity and superior damage resistance. In contrast, specimens with prefabricated hole-edge delamination exhibited reduced structural integrity, and delamination was more readily initiated from the prefabricated defects and propagated along the ply interfaces under loading. Among them, the specimen with a delamination diameter of 28 mm exhibited the most severe delamination, with pronounced thickness-direction swelling of the laminate, kink-band formation and fiber compression failure of the inner plies under severe compressive stress, accompanied by extensive interlaminar debonding. The coupling between interlaminar damage and intralaminar fiber/matrix damage accelerated the overall failure of the laminate. Notably, the delamination propagation direction exhibited a clear correlation with the adjacent ply orientations (ply 8 at −45° and ply 9 at 45°), which is consistent with the stress field distribution at the cohesive element interface.

As shown in the magnified view of the hole periphery in Fig. C, multiple failure modes were observed around the hole, including extensive matrix crushing and matrix cracking, accompanied by substantial fibre breakage and fiber-matrix shearing failure. This phenomenon was particularly pronounced in specimens with prefabricated hole-edge delamination.

In summary, the failure modes of the single-bolt double-shear specimens with hole-edge delamination are characterized by a combination of bearing failure, fibre breakage and buckling, matrix crushing and cracking, interlaminar delamination, and fiber-matrix shearing failure. These failure modes — fibre failure, matrix damage, and delamination — interact and couple with each other, collectively accelerating the damage and failure of the structure.

2.3.2 Ultimate Load-Bearing Capacity

The ultimate load data for all 12 specimens are presented in Table 2.3. The ultimate loads of the intact specimens were 16.34 kN, 16.77 kN and 16.21 kN, with an average of 16.44 kN; those of the 12 mm-delamination specimens were 16.11 kN, 16.03 kN and 15.96 kN, averaging 16.03 kN; those of the 20 mm-delamination specimens were 15.84 kN, 15.90 kN and 15.95 kN, averaging 15.89 kN; and those of the 28 mm-delamination specimens were 14.99 kN, 15.72 kN and 15.81 kN, averaging 15.51 kN. The average ultimate loads of the four specimen types were approximately 16 kN, with the intact specimens exhibiting the highest value (16.44 kN) and the 28 mm-delamination specimens the lowest (15.51 kN). Overall, the ultimate load decreased with increasing delamination diameter. Compared with the intact specimens, the average ultimate loads of the 12 mm, 20 mm and 28 mm delamination specimens decreased by 2.5%, 3.3% and 5.7%, respectively.

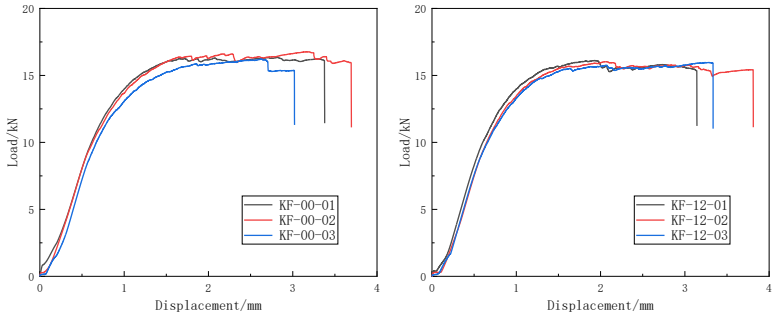
Table 2.3Ultimate loads of single-bolt double-shear specimens with hole-edge delamination

Delamination diameter/mm	Specimen designation	Ultimate load/kN	Average load/kN
0	KF-00-01	16.34	16.44
	KF-00-02	16.77	
	KF-00-03	16.21	
12	KF-12-01	16.11	16.03
	KF-12-02	16.03	
	KF-12-03	15.96	
20	KF-20-01	15.84	15.89
	KF-20-02	15.90	
	KF-20-03	15.95	
28	KF-28-01	14.99	15.51
	KF-28-02	15.72	
	KF-28-03	15.81	

These results indicate that prefabricated hole-edge delamination has a significant effect on the ultimate load-bearing capacity of the specimens; the larger the delamination diameter, the low3er the ultimate load and the lower the load-bearing capacity.

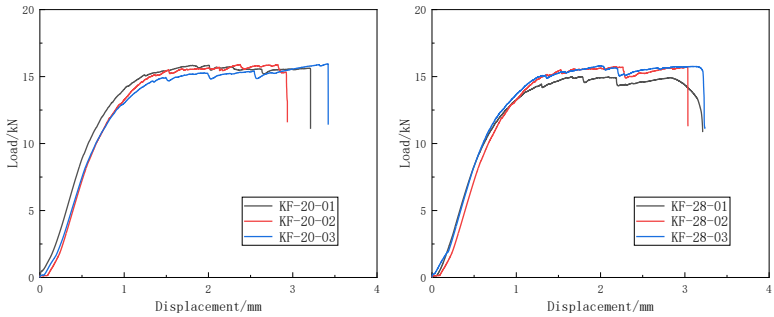
2.3.3 Load-Displacement Curve Analysis

The load-displacement curves of the four specimen types are presented in Fig. 2.9; for direct comparison, all curves are superimposed in Fig. 2.10. The four groups of curves exhibit highly similar trends, with excellent agreement among all 12 specimens, indicating that the mechanical behavior of this joint structure under tensile loading is stable and repeatable.



(Lift)Load-displacement curve of the intact specimen

(Right) Load-displacement curve of the specimen with delamination diameter of 12 mm



(Lift) Load-displacement curve of the specimen with delamination diameter of 20 mm

(Right) Load-displacement curve of the specimen with delamination diameter of 28 mm

Figure 2.9 Load-displacement curves of four types of composite single-bolt double-shear specimens with hole-edge delamination

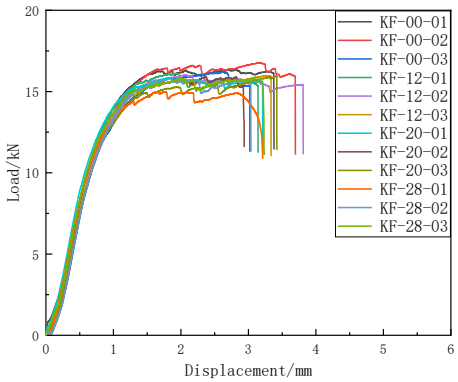


Figure 2.10 Load-displacement curves of all specimens

A representative curve was selected for detailed analysis, as shown in Fig. 2.11. The curve exhibits an overall nonlinear trend, and the failure process of the specimen can be characterized as a progressive accumulation of bearing damage around the hole. Based on the variation of the slope, the curve can be divided into four stages by points A, B and C: the initial nonlinear stage, the local damage initiation stage, the damage propagation stage, and the failure unloading stage.

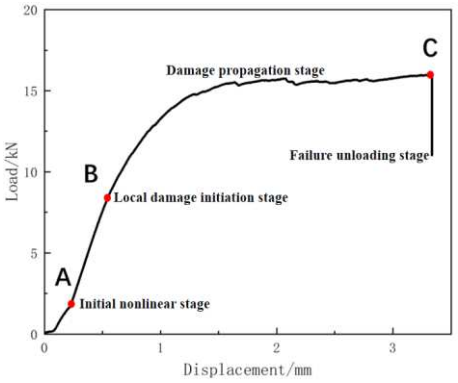


Figure 2.11 Load-displacement curve characteristics of the single-bolt double-shear specimen under tensile loading

The stage before point A is the initial nonlinear stage. Due to the initial clearance between the bolt and the hole in the laminate, contact between the bolt and the hole wall must first be established at the onset of loading, resulting in a slow load increase and a nonlinear curve.

The AB segment is the local damage initiation stage, characterized by a linear increase. During this stage, initial cracks begin to appear within the structure, such as fiber buckling and matrix cracking. However, these damages remain localized and do not significantly affect the macroscopic mechanical properties, which is reflected by the linear increase of load with displacement.

The BC segment is the damage propagation stage. As the load continues to increase, the internal damage gradually propagates and accumulates. Initial micro-cracks develop into extensive damage, including widespread fibre breakage, matrix crushing, and interlaminar debonding within the laminate. These failure modes — fibre failure, matrix damage, and delamination — interact and couple with each other, collectively promoting structural failure and substantially reducing the

load-bearing capacity of the structure. This stage exhibits pronounced nonlinear behavior and occupies the majority of the entire loading process.

Point C corresponds to the peak of the curve, representing the ultimate load, at which the load-bearing capacity of the structure reaches its maximum. Beyond this point, the structure undergoes global failure and enters the unloading stage, with a rapid decrease in load-bearing capacity.

In summary, the variation trend of the load-displacement curve corresponds to the damage and failure process of the structure, and the curve clearly characterizes the four stages of the tensile mechanical behavior of the single-bolt double-shear specimens with hole-edge delamination.

3.Progressive Damage Finite Element Model

Based on the experimental results presented in Chapter 2, a progressive damage finite element model is established in this chapter for the composite single-bolt double-shear joints with prefabricated hole-edge delamination. A UMAT subroutine is coded to implement the three-dimensional Hashin failure criterion and the Camanho degradation model. A mesh convergence study is then conducted to determine an appropriate mesh strategy. Subsequently, the finite element model is developed and numerical simulations are performed. The comparison between the simulated and experimental results will be detailed in Chapter 4. The overall analysis procedure is illustrated in Fig. 3.1.

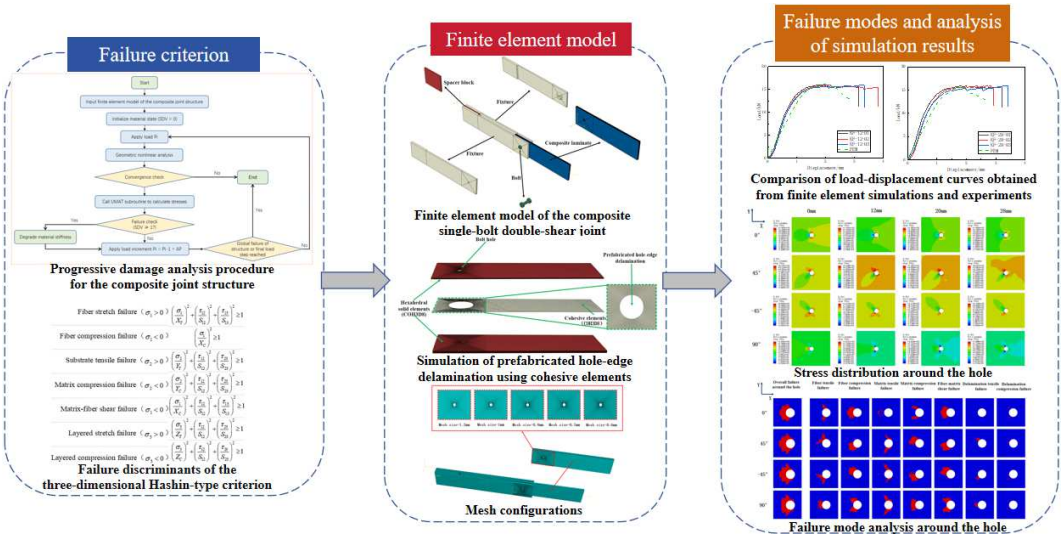


Fig. 3.1 Flowchart of the numerical simulation and validation procedure

3.1 Strength Failure Criterion

To accurately describe the damage initiation of composite laminates, the three-dimensional Hashin-type failure criterion improved by Tserpes is adopted in this study. This criterion classifies failure modes into seven categories, namely, fiber

tension/compression, matrix tension/compression, fiber-matrix shear, and delamination tension/compression, enabling a comprehensive description of the failure behavior of composites under complex stress states. Compared with other criteria such as the Puck criterion [46] and the Tsai-Wu criterion [47], the Hashin criterion [48] offers a distinct advantage in that it clearly differentiates various failure modes and provides corresponding physical failure criteria and stiffness degradation strategies for each mode, making it widely applicable in progressive damage analysis of composite materials.

The conventional two-dimensional Hashin criterion only incorporates four in-plane failure modes and cannot account for the stress effects in the thickness direction. For bolted joint structures, the region around the hole is subjected to significant stress components in the thickness direction in addition to in-plane loads, which may induce interlaminar failure. Tserpes et al. [49] introduced the normal and shear stress components in the thickness direction into the two-dimensional Hashin criterion and added three additional failure modes, i.e., delamination tension, delamination compression, and fiber-matrix shear failure, establishing a three-dimensional failure criterion that is more suitable for the failure analysis of joint structures with delamination damage. The failure discriminants for the seven failure modes are presented in Table 3.1.

Table 3.1 Failure discriminants of the three-dimensional Hashin-type criterion

Failuremode	**Failurediscriminant**	
Fiber stretch failure（$\sigma_1>0$）：	$\left(\frac{\sigma_1}{X_T}\right)^2+\left(\frac{\tau_{12}}{S_{12}}\right)^2+\left(\frac{\tau_{13}}{S_{13}}\right)^2\geq 1$	(3.1)
Fiber compression failure（$\sigma_1<0$）：	$\left(\frac{\sigma_1}{X_C}\right)^2\geq 1$	(3.2)
Substrate tensile failure（$\sigma_2>0$）：	$\left(\frac{\sigma_2}{Y_T}\right)^2+\left(\frac{\tau_{12}}{S_{12}}\right)^2+\left(\frac{\tau_{23}}{S_{23}}\right)^2\geq 1$	(3.3)
Matrix compression failure（$\sigma_2<0$）：	$\left(\frac{\sigma_2}{Y_C}\right)^2+\left(\frac{\tau_{12}}{S_{12}}\right)^2+\left(\frac{\tau_{23}}{S_{23}}\right)^2\geq 1$	(3.4)
Matrix-fiber shear failure（$\sigma_1<0$）：	$\left(\frac{\sigma_1}{X_C}\right)^2+\left(\frac{\tau_{12}}{S_{12}}\right)^2+\left(\frac{\tau_{13}}{S_{13}}\right)^2\geq 1$	(3.5)
Layered stretch failure（$\sigma_3>0$）：	$\left(\frac{\sigma_3}{Z_T}\right)^2+\left(\frac{\tau_{12}}{S_{12}}\right)^2+\left(\frac{\tau_{23}}{S_{23}}\right)^2\geq 1$	(3.6)
Layered compression failure（$\sigma_3<0$）：	$\left(\frac{\sigma_3}{Z_C}\right)^2+\left(\frac{\tau_{12}}{S_{12}}\right)^2+\left(\frac{\tau_{23}}{S_{23}}\right)^2\geq 1$	(3.7)

In the above expressions, σ_1, σ_2 and σ_3 denote the normal stresses in the fiber direction, matrix direction, and normal direction, respectively; τ_{12}, τ_{13}, and τ_{23} are the shear stresses in the corresponding planes; X_T and X_C are the tensile and compressive strengths in the fiber direction; Y_T and Y_C are the tensile and compressive strengths in the matrix direction; Z_T and Z_C are the tensile and compressive strengths in the normal direction; and S_{12}, S_{13}, and S_{23} are the shear strengths in the corresponding planes.

3.2 Material Degradation Model

When any failure criterion is satisfied in an element, its stiffness must be degraded to simulate the degradation of material performance. Commonly used material degradation models include the instantaneous failure model, progressive failure model, and constant stress failure model. The instantaneous failure model reduces the stiffness of failed elements directly to zero. Due to its simplicity, it has been widely adopted in studies by Tan [50], Chang and Chang [51], and McCarthy et al. [52]. The progressive failure model, on the other hand, degrades the stiffness gradually to simulate the process of damage evolution.

In this study, the Camanho degradation model modified by Tserpes is employed [53]. This model assigns different degradation factors to different failure modes, which not only captures the physical distinctions among various damage modes but also maintains computational efficiency. The specific degradation factors are listed in Table 3.2. The degraded stiffness matrix is then used in the stress calculation of the subsequent increment step to achieve progressive loss of material stiffness.

Table 3.2 Stiffness degradation factors of the modified Camanho model

Failure mode	E_1	E_2	E_3	G_{12}	G_{13}	G_{23}	ν_{12}	ν_{13}	ν_{23}
Fiber stretch failure	0.07	0.07	0.07	0.07	0.07	0.07	0.07	0.07	0.07
Fiber compression failure	0.14	0.14	0.14	0.14	0.14	0.14	0.14	0.14	0.14
Matrix tensile failure		0.2		0.2		0.2			
Matrix compression failure		0.4		0.4		0.4			
Fiber-matrix shear failure				0.1			0.1		
Delamination tensile failure			0.2		0.2	0.2		0.2	0.2
Delamination compression failure			0.2		0.2	0.2		0.2	0.2

3.3 Finite Element Implementation Based on UMAT Subroutine

The three-dimensional Hashin failure criterion and Camanho degradation model described above were coded in Fortran as a UMAT (User-defined Material) subroutine within the ABAQUS finite element software to perform stress updating and material state evolution in the progressive damage analysis of the joint structure.

ABAQUS provides two types of user material subroutines: UMAT for the Standard implicit solver, which is suitable for iterative solutions of static and quasi-static problems, and VUMAT for the Explicit solver, which is designed for dynamic problems such as high-velocity impact and collision. Since the present study focuses on the quasi-static tensile response of composite single-bolt double-shear joints without involving dynamic effects, the UMAT subroutine is selected.

Within the UMAT subroutine, the material Jacobian matrix, that is, the derivative of the stress increment with respect to the strain increment in the current increment step, must be provided for global stiffness assembly and iterative convergence in the implicit solution procedure. For damaged materials, the Jacobian matrix can be expressed as:

$$\frac{\partial \sigma}{\partial \varepsilon} = C_d + \frac{\partial C_d}{\partial \varepsilon} : \varepsilon \tag{3.7}$$

Where C_d is the material stiffness matrix in the damaged state, the specific expression of which is determined by the current failure mode(s) and the corresponding degradation factors.

In terms of numerical implementation, seven solution-dependent state variables (SDVs) were defined in the UMAT subroutine to flag the activation states of the seven failure modes, including fiber tension/compression, matrix tension/compression, fiber-matrix shear, and delamination tension/compression, with a value of 0 indicating inactive and 1 indicating active. At each increment step, the UMAT subroutine first updates the stress field based on the strain increment, and then evaluates the seven failure criteria sequentially. If any failure criterion is satisfied, the corresponding stiffness components are degraded according to the Camanho degradation model (Table 3.2), the Jacobian matrix and stresses are updated, and the corresponding SDV is set to 1 to mark the occurrence of that failure mode in the element. If multiple failure modes occur simultaneously, degradation is applied sequentially in order. This procedure is repeated at all integration points in each increment step until convergence is achieved or the termination condition is reached. The overall procedure of the progressive damage analysis is illustrated in Fig. 3.2.

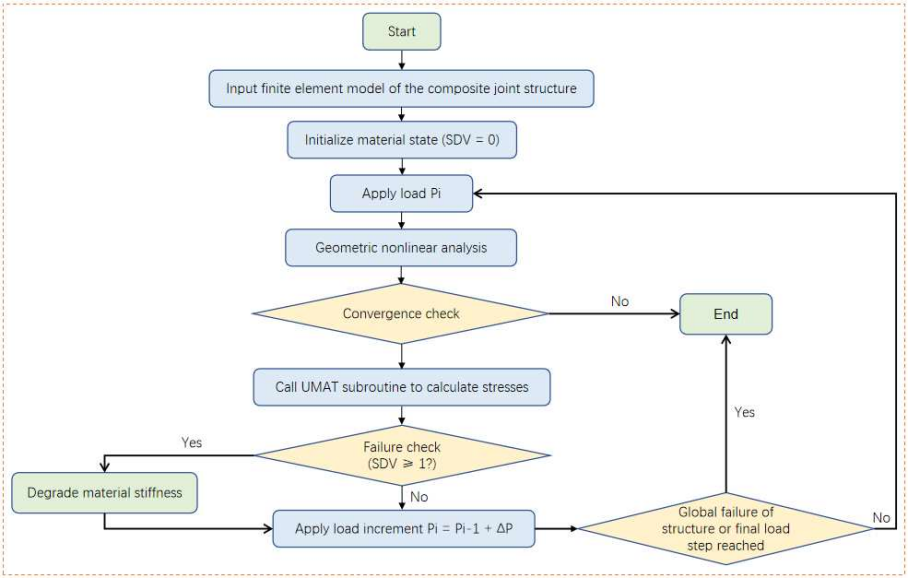


Figure 3.2 Progressive damage analysis procedure for the composite joint structure

The stress update procedure within the UMAT subroutine is shown in Fig. 3.3.

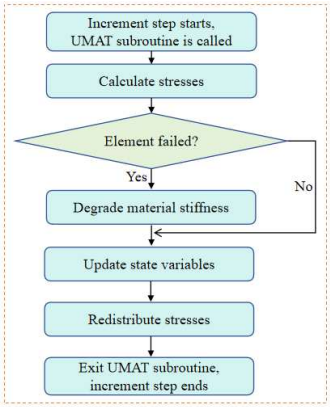


Figure 3.3 Stress calculation process via UMAT subroutine

3.4 Cohesive Zone Delamination Model

To simulate the initiation and propagation of prefabricated hole-edge delamination under tensile loading, the cohesive zone model (CZM) is adopted to describe the interlaminar interfacial behavior. Compared with the virtual crack closure technique (VCCT) and the extended finite element method (XFEM), the CZM offers advantages in that it does not require pre-existing initial cracks to predict delamination initiation and can simultaneously simulate three crack propagation modes, that is, mode I (opening mode), mode II (sliding mode), and mode III (tearing mode). It is therefore more suitable for the joint structure with prefabricated delamination defects in the present study.

The cohesive constitutive relation is represented by a bilinear traction-separation model, as shown in Fig. 3.4. In the figure, the horizontal axis denotes the separation displacement and the vertical axis denotes the interfacial traction. Figs. 3.4(a), (b), and (c) correspond to the normal, shear, and mixed-mode behaviors, respectively. Before damage initiation, the interface is in the linear elastic stage, and the slope of the curve represents the initial stiffness K_n^0. When the traction reaches the interfacial strength t_n^0, delamination initiates, with the corresponding separation displacement denoted as δ_n^0. Thereafter, the traction gradually decreases with increasing separation displacement, that is, stiffness degradation occurs, until the separation displacement reaches δ_n^f, where the traction drops to zero and the element completely fails.

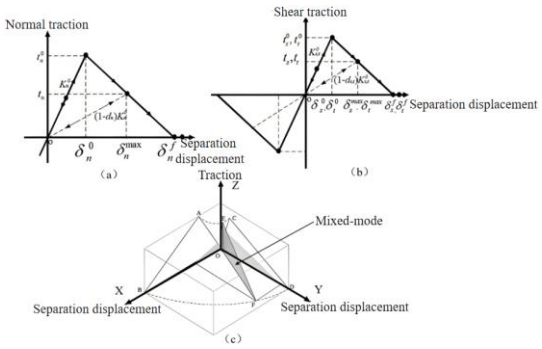


Figure 3.4 Bilinear cohesive zone constitutive model

The cohesive constitutive relation can be expressed as:

$$\begin{Bmatrix} t_n \\ t_s \\ t_t \end{Bmatrix} = \begin{bmatrix} K_n & & \\ & K_s & \\ & & K_t \end{bmatrix} \begin{bmatrix} \delta_n \\ \delta_s \\ \delta_t \end{bmatrix} \tag{3.8}$$

where t_n , t_s , and t_t are the tractions in the normal and two shear directions, respectively; δ_n , δ_s , and δ_t are the corresponding separation displacements; and K_n , K_s , and K_t are the interfacial stiffnesses in the three directions.

After damage initiation, the interfacial stiffness is degraded as follows:

where the braces K_i （$i = n,s,t$）denote：

$$K_i = \begin{cases} K_i^0 & \delta_i \le \delta_i^0 \\ (1-d_i)K_i^0 & \delta_i^0 \le \delta_i \le \delta_i^f \\ 0 & \delta_i \ge \delta_i^f \end{cases} \quad i = n,s,t \tag{3.9}$$

where K_i^0 is the initial interfacial stiffness, δ_i^0 and δ_i^f are the effective displacements at damage initiation and complete failure, respectively, and d_i is the damage variable for delamination propagation. The damage variable in the above equation is expressed as:

$$d = \frac{\delta^f \left(\delta^{\max} - \delta^0\right)}{\delta^{\max}\left(\delta^f - \delta^0\right)} \tag{3.10}$$

where δ^f is the effective displacement at complete failure, δ^0 is the effective displacement at damage initiation, $\delta^f = 2G_C / t_i^0 \left(i = n,s,t\right)$ and $\delta^{\max}$ is the maximum effective displacement during the loading history.

In this study, the quadratic nominal stress criterion is employed to determine delamination initiation. This criterion accounts for the coupling effects among the traction components in the three directions and is expressed as:

$$\left\{\frac{\langle t_n \rangle}{t_n^0}\right\}^2 + \left\{\frac{t_s}{t_s^0}\right\}^2 + \left\{\frac{t_t}{t_t^0}\right\}^2 = 1 \tag{3.11}$$

When the above equation is satisfied, delamination initiation occurs. In the equation, the Macaulay brackets < > indicate that delamination does not occur under pure compressive stress states.

The delamination propagation is governed by the power-law criterion based on fracture energy [54-55], which is expressed as:

$$\left(\frac{G_I}{G_{IC}}\right)^\beta + \left(\frac{G_{II}}{G_{IIC}}\right)^\beta + \left(\frac{G_{III}}{G_{IIIC}}\right)^\beta = 1 \tag{3.12}$$

where G_I, G_{II}, and G_{III} are the energy release rates for the three crack propagation modes; G_{IC}, G_{IIC}, and G_{IIIC} are the corresponding critical fracture energies; and β is a coupling parameter describing the interaction among the three propagation modes, typically taking values of 1 or 2. In this study, β =2.

Since the computational accuracy and stability of cohesive elements are influenced by multiple parameters, the selection of the key parameters is discussed below.

(1) Cohesive element size

To accurately capture the stress gradient at the delamination front, the cohesive element size should be sufficiently small. According to the estimation method proposed by Hillerborg et al. [56], the cohesive element size l_{ce} is related to the number of elements N_{cz} and the length of the cohesive zone l_{cz} by $l_{ce} = l_{cz} / N_{cz}$. The cohesive zone length can be estimated as:

$$l_{cz} = \alpha E_{iso} \frac{G_{C,iso}}{\left(\tau^0\right)^2} \tag{3.13}$$

where E_{iso} is the elastic modulus, $G_{C,iso}$ is the critical strain energy release rate, τ^0 is the interfacial strength, and α is a parameter related to the cohesive model with a value less than 1. Regarding the number of cohesive elements, Harper et al. [57] suggested that α should be in the range of 1.2 to 2.4 for mode I delamination, 2.05 to 2.73 for mode II delamination, and 1.5 to 3.5 for mixed-mode delamination.

(2) Interfacial stiffness

The interfacial stiffness should bechosen within a reasonable range. Excessively large values may lead to convergence difficulties, while excessively small values may reduce the overall stiffness of the laminate. In this study, the interfacial stiffness is estimated based on classical fracture mechanics, determined by the fracture energy, failure displacement, and damage initiation ratio to ensure computational stability. The following estimation method can be adopted, where the interfacial stiffness *K* is a function of the fracture energy G_c, the failure displacement δ_f, and the damage initiation δ_{ratio}:

$$K = \frac{2G_c}{\delta_{ratio}\delta_f^2} T^0 \tag{3.14}$$

where the damage initiation ratio $\delta_{ratio} = \delta_0 / \delta_f$ is the separation displacement at damage initiation, δ_0 is the separation displacement at complete failure, and T_0 is the thickness of the cohesive element, which is typically set to 1. The value of δ_{ratio} is usually taken as 0.5.

(3) Interfacial strength

For most composite material systems, the interfacial strength is difficult to determine directly through experiments. Based on the traction-separation relationship, the interfacial strength τ^0 can be expressed as a function of the fracture energy G_c and the failure displacement δ_f :

$$\tau^0 = \frac{2G_c}{\delta_f} \tag{3.15}$$

According to classical fracture mechanics, a smaller failure displacement δfδf is preferable. However, if δ_f is too small, the computational accuracy may be compromised. In practice, δ_f is often taken as a certain percentage of the cohesive element size, and the element size should ensure that 3 to 5 elements are placed within the delamination front zone. Soden et al. [58] suggested that taking δ_f as 5% of the cohesive element size yields satisfactory computational accuracy.

(4) Viscosity coefficient

Stiffness degradation of composite materials during loading often causes convergence difficulties for cohesive elements. The introduction of a viscosity coefficient in finite element analysis can effectively improve convergence behavior. However, its value should be determined by balancing computational cost, accuracy, and convergence. Existing studies suggest that a viscosity coefficient in the range of 10^{-5}-10^{-3} can effectively enhance convergence without significantly affecting the computational results.

3.5 Finite Element Modeling of the Single-Bolt Double-Shear Joint

3.5.1 Geometric Model

Based on the specimen dimensions described in Chapter 2, a three-dimensional finite element model of the composite single-bolt double-shear joint was established in ABAQUS, as shown in Fig. 3.5. The model consisted of the composite laminate, bolt, nut, washer, and metallic fixture components (including loading plates and a spacer block). The laminate was partitioned ply-by-ply in the thickness direction according to the actual number of plies (24 plies) to ensure that each ply could be assigned independent material orientations and failure criteria. The bolt was modeled as a smooth shank without considering thread details to improve computational efficiency.

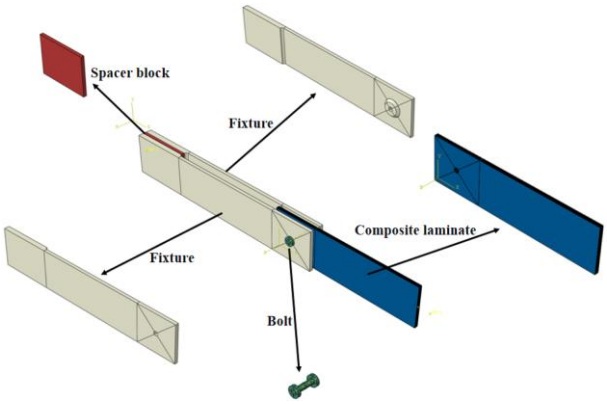


Fig. 3.5 Finite element model of the composite single-bolt double-shear joint

3.5.2 Element Type and Mesh Generation

All components were meshed using eight-node linear hexahedral elements with reduced integration (C3D8R). This element type is less susceptible to shear locking in bending problems, and the reduced integration scheme effectively controls computational cost. However, hourglassing issues may arise, and thus the enhanced hourglass control option was activated in the analysis.

The region around the hole in the laminate, where stress concentration and damage initiation are critical, was locally refined, while coarser meshes were used in regions away from the hole periphery to control the total number of elements, as shown in Fig. 3.6.

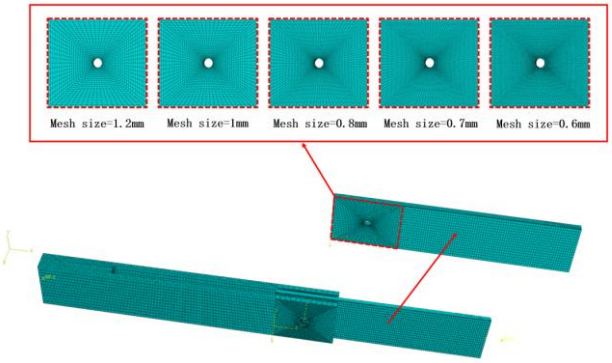


Fig. 3.6 Mesh configurations of the single-bolt double-shear joint with different element sizes

A systematic mesh convergence study was conducted to determine an appropriate mesh density. The global mesh size was fixed at 1.2 mm, and five local mesh sizes of 1.2 mm, 1.0 mm, 0.8 mm, 0.7 mm, and 0.6 mm were applied to the hole periphery. The load-displacement curves obtained with the five mesh sizes are compared in Fig. 3.7. The results indicated that the deviation between the 1.2 mm and 1.0 mm mesh sizes was relatively large. When the local mesh was refined to 0.8 mm, further refinement to 0.7 mm and 0.6 mm resulted in only minor changes in the ultimate load and curve shape, demonstrating that the 0.8 mm mesh already satisfies the accuracy requirements. Considering both accuracy and efficiency, a global mesh size of 1.2 mm with a local refined mesh size of 0.8 mm around the hole was adopted, resulting in a total of 110570 elements.

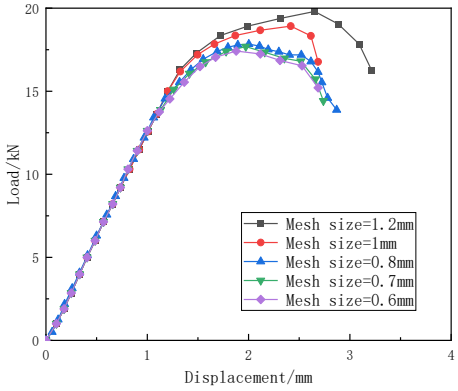


Fig. 3.7 Load-displacement curves of the single-bolt double-shear joint with different mesh sizes

To model the prefabricated hole-edge delamination, zero-thickness cohesive elements (COH3D8) were inserted between the 8th and 9th plies, as shown in Fig. 3.8.

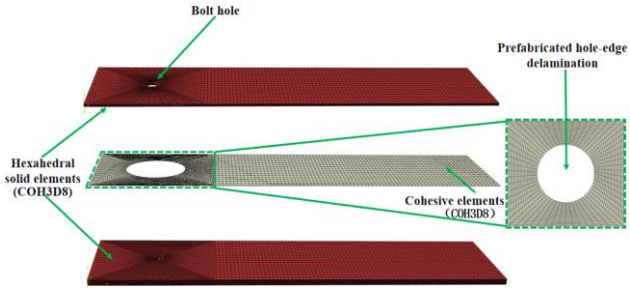


Fig. 3.8 Simulation of prefabricated hole-edge delamination using cohesive elements

3.5.3 Material Properties

The laminate material used in this study was ZT7H3194U/QY9512 carbon fiber/epoxy composite, and its elastic constants, strength parameters, and layup information are listed in Table 3.3. The fixture and bolt materials were both 30CrMnSiA steel, with an elastic modulus of 210 GPa and a Poisson's ratio of 0.3.

Table 3.3 Material properties of ZT7H3194U/QY9512 carbon fiber/epoxy composite laminate

Materialparameter	Value	Description
E_{11}	146（GPa）	Longitudinal elastic modulus
E_{22}、E_{33}	10.4（GPa）	Transverse and normal elastic moduli
G_{12}、G_{23}、G_{13}	6.45（GPa）	In-plane shear moduli in 12, 23, and 13 planes
ν_{12}、ν_{13}	0.28	Poisson's ratios in 12 and 13 planes
ν_{23}	0.3	Poisson's ratio in 23 plane
X_T	2390 （MPa）	Longitudinal tensile strength
X_C	1410（MPa）	Longitudinal compressive strength
Y_T	67.6（MPa）	Transverse tensile strength
Y_C	219（MPa）	Transverse compressive strength
Z_T	67.6（MPa）	Normal tensile strength
Z_C	219（MPa）	Normal compressive strength
S_{12}、S_{23}、S_{13}	94.8（MPa）	Shear strengths in 12, 23, and 13 planes

The interfacial properties of the cohesive elements are presented in Table 3.4, where τ_{nn}^{0}, τ_{ss}^{0}, and τ_{tt}^{0} denote the interfacial strengths in the normal and two shear directions, and K_{nn}, K_{ss}, and K_{tt} denote the corresponding interfacial stiffnesses.

Table 3.4 Mechanical properties of cohesive elements

τ_{nn}^{0} / MPa	τ_{ss}^{0} / MPa	τ_{tt}^{0} / MPa	K_{nn} / MPa	K_{ss} / MPa	K_{tt} / MPa
6.56	44.4	44.4	524.8	3552	3552

3.5.4 Contact Definitions

A total of seven contact pairs were defined in the model to describe the contact interactions between bolt and hole wall, bolt and washer, washer and laminate surface, laminate and fixture, as well as among the fixture components themselves. The contact properties were defined following the master-slave principle: the surfaces of the stiffer metallic components were designated as master surfaces, while the composite laminate surfaces were designated as slave surfaces. The normal contact behavior was modeled as hard contact, and the tangential behavior was modeled using the penalty friction method with a friction coefficient of 0.1.

3.5.5 Loads and Boundary Conditions

Fixed boundary conditions (all translational and rotational degrees of freedom constrained) were applied to the fixture end, and a displacement load was applied to the tensile end of the laminate through a reference point, as shown in Fig. 3.9.

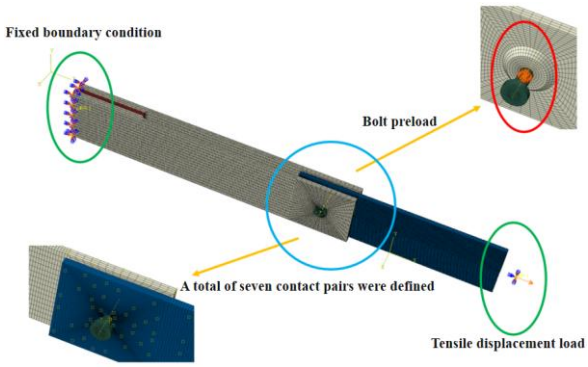


Fig. 3.9 Load and boundary condition setup for the composite single-bolt double-shear joint

The loading process was divided into five steps to achieve smooth application of bolt preload and subsequent tensile loading: (1) an initial preload of 10 N was applied to establish preliminary contact between the bolt and the hole wall, as well as between the bolt and the fixture; (2) the fixed constraint at the laminate end was deactivated; (3) The target preload of 4250 N was applied, which was determined from the experimental tightening torque T = 3.4 N·m using the following relationship with a torque coefficient K = 0.2 and a nominal bolt diameter D = 4 mm; (4) the bolt length was fixed (changing the bolt load status from "apply preload" to "fix at current length"); (5) a displacement load of 4 mm was applied to the tensile end of the laminate until structural failure occurred.

$$T = K \times Q_P \times d \tag{3.16}$$

Where T is the tightening torque, Q_P is the bolt preload, d is the bolt diameter, and K is the torque coefficient, which is taken as 0.2 in this study.

3.5.6 Solver Settings and Convergence Measures

In this study, the ABAQUS/Standard implicit solver was used for quasi-static analysis. Due to the presence of complex contact nonlinearities and material nonlinearities (stiffness degradation) in the model, the following measures were taken to ensure convergence: (1) geometric nonlinearity (NLGEOM) was activated to account for large displacement effects; (2) the initial increment size was set to 0.05, the minimum increment size to 10^{-8}, and the maximum increment size to 0.1, to smoothly track the damage evolution process; (3) for the cohesive elements, viscosity regularization was introduced to alleviate convergence difficulties during stiffness degradation.

4.Results and Discussion

4.1 Comparison between Finite Element Simulation and Experimental Results

4.1.1 Comparison of Ultimate Loads

The ultimate loads of the single-bolt double-shear specimens with hole-edge delamination were obtained from the finite element simulations using the model established in this study. The comparison between the simulated and experimental ultimate loads is presented in Table 4.1.

Table 4.1 Comparison of simulated and experimental ultimate loads of single-bolt double-shear joints with hole-edge delamination

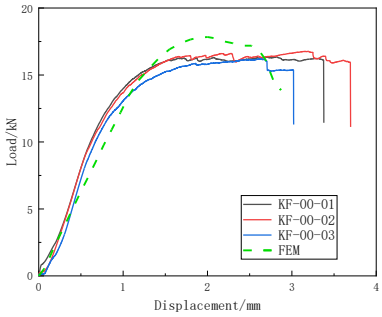
Delamination/mm	Simulated ultimate load/kN	Experimental ultimate load/kN	Error/%
0	17.83	16.44	8.4
12	16.16	16.03	0.8
20	15.61	15.89	-1.8
28	14.96	15.51	-3.7

The relative errors between the simulated and experimental values for the four types of delamination specimens are all within 10%, demonstrating that the finite element results are in good agreement with the experimental results, which validates the effectiveness and accuracy of the finite element simulation method established in this study.

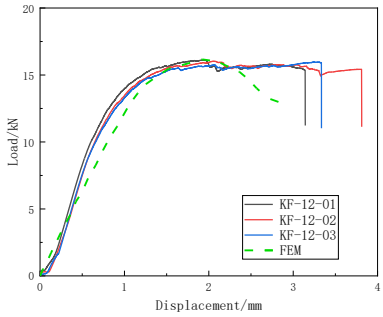
As the delamination diameter increases, the simulated ultimate load decreases accordingly, and this trend is consistent with the experimental results. This further indicates that prefabricated hole-edge delamination has a significant effect on the load-bearing capacity of the joint structure. With increasing delamination diameter, the ultimate load of the joint decreases, and the ultimate load-bearing capacity is reduced correspondingly.

4.1.2 Comparison of Load-Displacement Curves

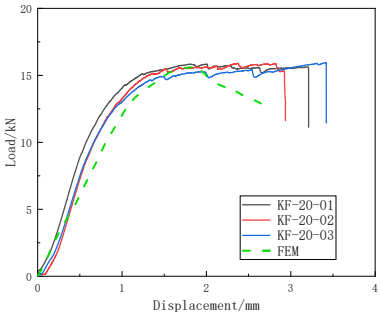
The load-displacement curves obtained from the finite element simulations and those from the experiments are compared in Fig. 4.1, where the green dashed lines represent the finite element results. It can be observed that the finite element results are in good agreement with the experimental results, and the overall trends are generally consistent. Corresponding to the four stages identified from the experimental curves in Fig. 2.10 of Chapter 2, in the early elastic stage, the load increases linearly with displacement. After reaching a certain load level, the linear stage ends and the curve transitions to a nonlinear increasing trend. When the load reaches the ultimate load, the load-bearing capacity of the structure reaches its maximum, after which the curve begins to descend and the load-bearing capacity decreases until final failure occurs.



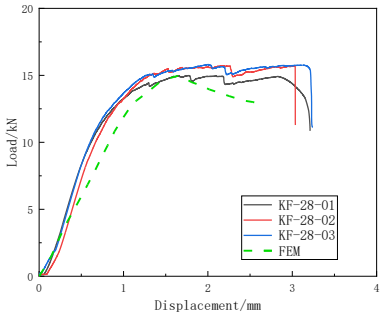
(a) Intact specimen



(b) Specimen with 12 mm delamination diameter



(c) Specimen with 20 mm delamination diameter



(d) Specimen with 28 mm delamination diameter

Fig. 4.1 Comparison of load-displacement curves obtained from finite element simulations and experiments for four delamination diameters

The load-displacement curves obtained from finite element simulations for the four delamination diameters are shown in Fig. 4.2. It can be seen that as the delamination diameter increases, the curves exhibit very good consistency in the initial linear stage, indicating that the delamination diameter has little effect on the initial stiffness of the structure. Furthermore, as the delamination diameter increases, the ultimate load decreases, and this trend is also consistent with the experimental results, which further verifies the accuracy of the finite element method. Meanwhile, as the delamination diameter increases, the ductility of the structure decreases to a certain extent.

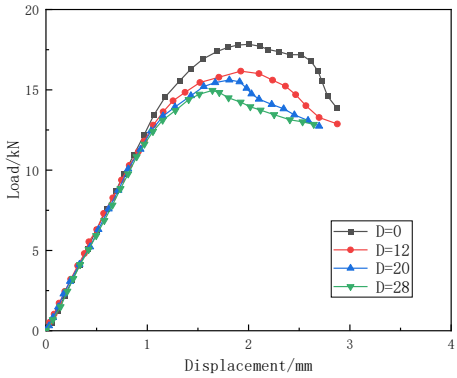


Fig. 4.2 Comparison of load-displacement curves obtained from finite element simulations for different delamination diameters

4.1.3 Stress Analysis Around the Hole

Fig. 4.3 presents the Mises stress distributions around the hole at different ply orientations for various delamination diameters. It can be observed that under tensile loading, bearing deformation occurs around the hole in the joint structure. A significant stress concentration appears on the compression side, where the stress amplitude increases sharply, while no significant stress variation is observed on the opposite side, where the stress amplitude remains relatively low.

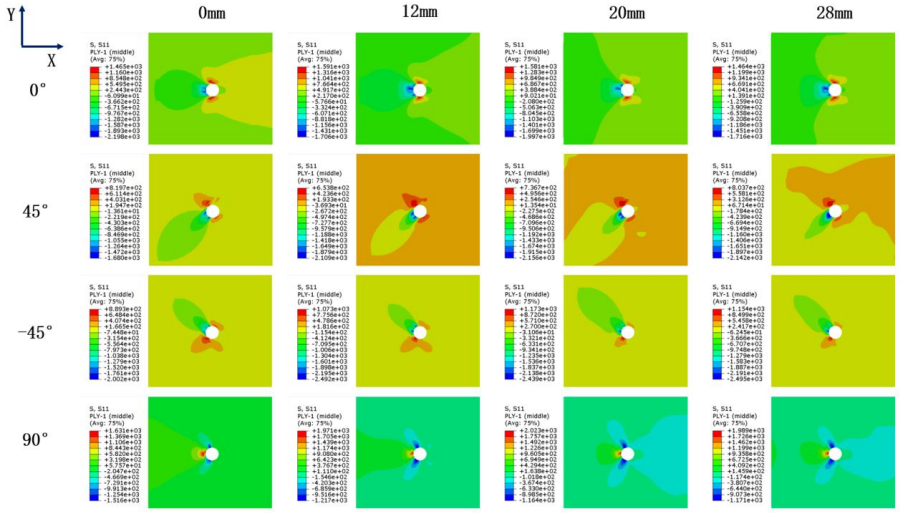


Fig. 4.3 Stress distribution around the hole in the single-bolt double-shear joint

As the delamination diameter increases, the stress values at each ply orientation increase to a certain extent. The intact specimen exhibits the lowest stress values, while the stress values of the delaminated specimens increase progressively with the delamination diameter, indicating that a larger delamination diameter leads to more pronounced stress concentration in the delamination region, which is consistent with the variation of load-bearing capacity.

Distinct differences in stress distribution are observed among different ply orientations. The stress amplitudes of the 0° and 90° plies are larger than those of the 45° and -45° plies, indicating that the 0° and 90° plies have higher stress-bearing capacity. The stress distributions in the 45° and -45° plies exhibit clear symmetry, with stresses concentrated in the fiber directions (45° and -45°). For the 0° and 90° plies, stresses are also mainly concentrated in the fiber directions, while a certain

range of stress also exists in the direction perpendicular to the fibers. This phenomenon is mainly attributed to the combined effects of the loading direction and the difference in elastic modulus between the fibers and the matrix.

4.1.4 Failure Mode Analysis Around the Hole

Through the seven solution-dependent state variables (SDV) defined in the UMAT subroutine, the distribution contours of seven failure modes, namely fiber tension/compression, matrix tension/compression, fiber-matrix shear, and delamination tension/compression, can be output. Fig. 4.4 presents the failure mode distributions around the hole at different ply orientations, and Fig. 4.5 presents the interlaminar failure mode distributions around the hole for different delamination diameters.

It can be seen from Fig. 4.4 that damage initiates from the compression side of the hole edge and propagates outward in a radial pattern at each ply orientation. The dominant failure modes are fiber compression failure, matrix compression failure, and fiber-matrix shear failure, which are highly concentrated on the compression side. Fiber tensile failure and matrix tensile failure only appear locally, while delamination tensile and delamination compression failures are the most limited in distribution. Due to the bearing effect at the hole edge, distinct matrix compression failure and fiber compression failure occur in the bearing zone of each ply, indicating that the specimen undergoes significant damage in the bearing zone, resulting in a typical bearing failure mode, which is consistent with the experimental results. The failure zone caused by compression is much larger than that caused by tension, indicating that the fibers bear most of the load while the matrix has relatively weak load-bearing capacity.

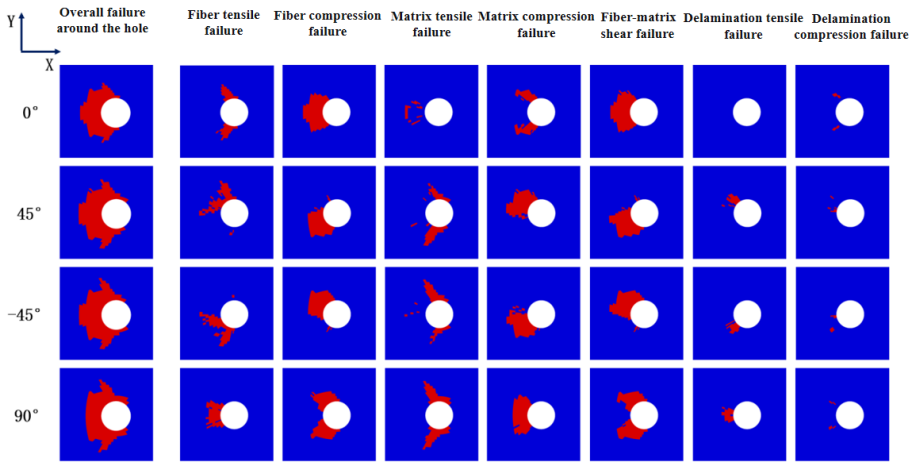


Fig. 4.4 Failure mode analysis around the hole at different ply orientations

Regular differences are observed among different ply orientations. The 45° and -45° plies exhibit clear symmetry in all failure modes, with damage distributed along the ±45° directions, which is consistent with the stress distribution results. The failure mode distributions of the 0° and 90° plies are perpendicular to each other, which is related to the fact that the two ply orientations are perpendicular to each other.

It can be seen from Fig. 4.5 that as the delamination diameter increases, the distribution range of interlaminar failure modes tends to expand. Matrix compression failure and fiber-matrix shear failure are most concentrated in the interlaminar

distribution, accumulating extensively on the compression side. Under the 28 mm delamination diameter condition, fiber compression failure, fiber-matrix shear failure, and delamination compression failure all show a significant increase compared with the intact specimen, indicating that a larger hole-edge delamination diameter exacerbates the propagation of interlaminar damage.

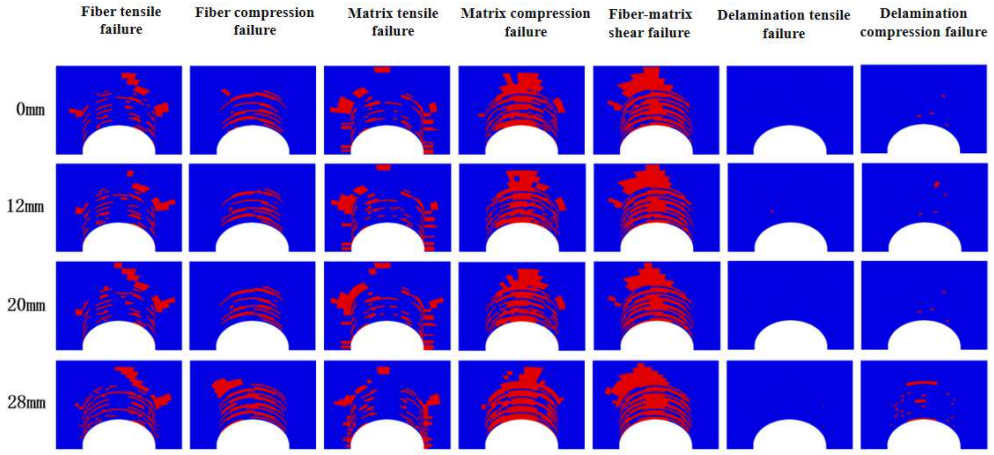
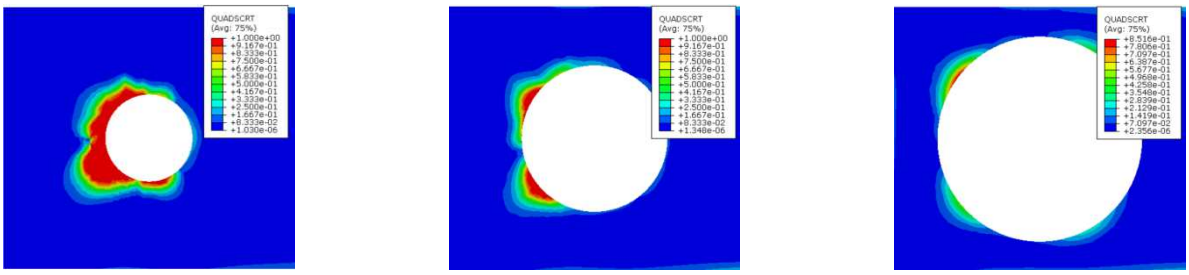


Fig. 4.5 Interlaminar failure mode analysis around the hole for different delamination diameters

4.1.5 Delamination Propagation Mechanism Analysis

In addition to intralaminar fiber and matrix damage, the failure of the joint structure under external loading is also accompanied by interlaminar delamination propagation. In this study, zero-thickness cohesive elements are used to simulate the prefabricated delamination, and the damage state of the elements is characterized by the QUADSCRT value: QUADSCRT < 1 indicates that the cohesive element is in the elastic stage without damage, and QUADSCRT = 1 indicates that complete damage has occurred. Fig. 4.6 presents the damage propagation contours of cohesive elements for three prefabricated delamination diameters.



(a) 12 mm prefabricated delamination (b) 20 mm prefabricated delamination (c) 28 mm prefabricated delamination

Fig. 4.6 Delamination propagation for different delamination diameters

Delamination mainly initiates from the compression side of the hole edge and propagates outward in a semi-circular pattern (particularly evident under the 20 mm prefabricated delamination condition), while almost no damage occurs on the opposite side, which is consistent with the distribution of other failure modes around the hole. The direction of damage propagation is mainly concentrated in the ±45° directions. This is because the prefabricated delamination is located at one-

third of the laminate thickness, that is, between the 8th ply (-45°) and the 9th ply (45°), indicating that the propagation direction of the cohesive elements is correlated with the orientations of the adjacent plies.

The delamination propagation range varies with different delamination diameters. The propagation range is largest under the 12 mm prefabricated delamination and smallest under the 28 mm prefabricated delamination. The 12 mm prefabricated delamination is relatively small, and under external loading, the delamination damage covers the prefabricated region and then continues to propagate outward along the hole periphery. The 28 mm prefabricated delamination is relatively large, and the delamination damage first occurs within the prefabricated region; only after complete coverage of the prefabricated region does a small amount of propagation occur outside it.

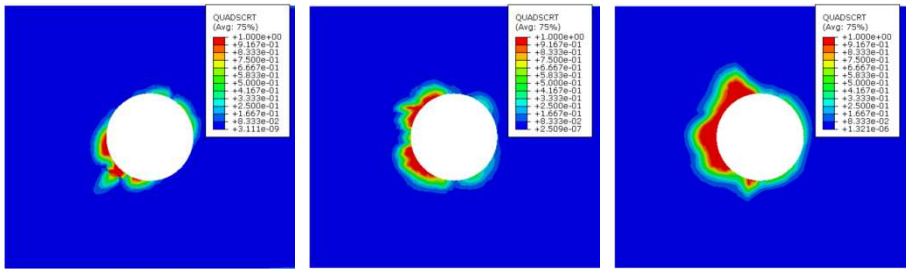
4.2 Effects of Different Hole-Edge Delamination Parameters on Damage and Failure of Single-Bolt Double-Shear Joints

In addition to the delamination diameter, parameters such as the location, shape, and orientation of the hole-edge delamination also affect the mechanical performance of the joint structure. Based on the finite element model established in this study, this section further investigates the effects of these three delamination parameters on the damage and failure of the joint structure.

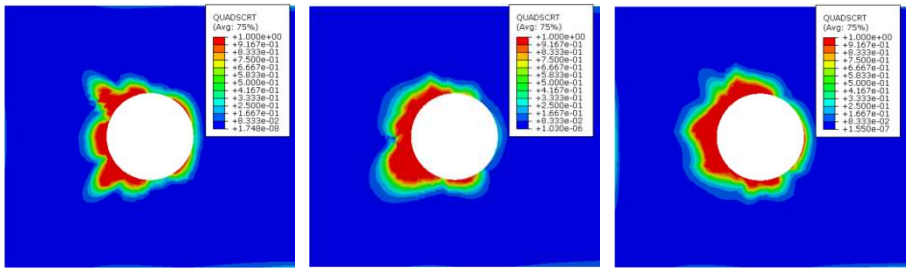
4.2.1 Effect of Delamination Location

Using the 12 mm circular prefabricated delamination as the baseline, prefabricated delamination was introduced at six locations along the laminate thickness direction, namely at 1/24, 1/12, 1/6, 1/4, 1/3, and 1/2 of the thickness (corresponding to between plies 1-2, 2-3, 4-5, 6-7, 8-9, and 12-13, respectively), to analyze the effect of delamination location on the joint structure.

The delamination propagation of cohesive elements under different delamination locations is shown in Fig. 4.7. The propagation range is smaller for plies closer to the laminate surface (e.g., plies 1-2). As the delamination location moves toward the interior of the laminate, the propagation range gradually increases. When the delamination is located at plies 12-13, the propagation range reaches its maximum. This indicates that the lateral constraint of the bolt preload suppresses delamination propagation to a certain extent in the surface plies, while the constraint is weaker in the middle of the laminate due to the greater distance from the bolt, resulting in more pronounced delamination propagation.



(a) Plies 1-2 (b) Plies 2-3 (c) Plies 4-5



(d) Plies 6-7 (e) Plies 8-9 (f) Plies 12-13

Fig. 4.7 Delamination propagation at different delamination locations

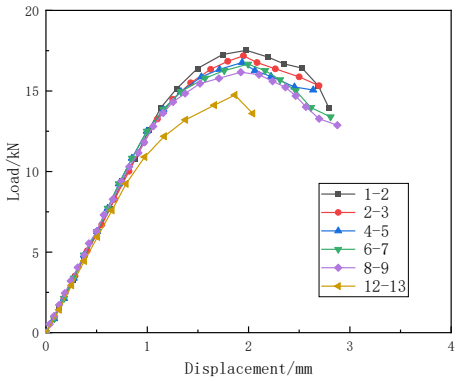


Fig. 4.8 Comparison of load-displacement curves obtained from finite element simulations for different delamination locations

The load-displacement curves for different delamination locations are shown in Fig. 4.8. The overall trends of the curves are similar, with good consistency in the initial linear stage, indicating that the change in delamination location has little effect on the overall stiffness of the structure. The comparison of ultimate load-bearing capacity under different delamination locations is shown in Fig. 4.9. When the delamination is located at the surface plies (plies 1-2), the ultimate load is the largest. As the delamination location moves inward, the load-bearing capacity gradually decreases. When the delamination is located at plies 12-13, the load-bearing capacity reaches its minimum, which is consistent with the delamination propagation behavior.

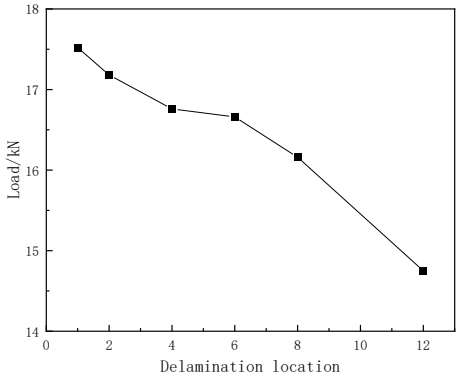
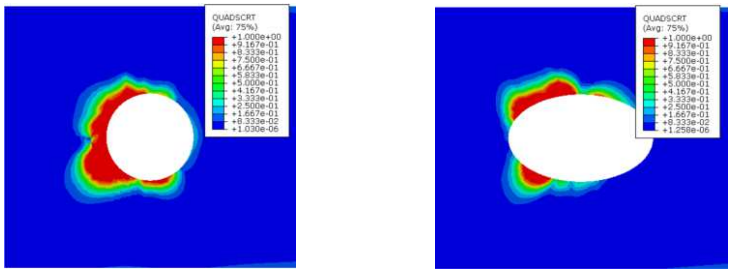


Fig. 4.9 Comparison of ultimate load-bearing capacity at different delamination locations

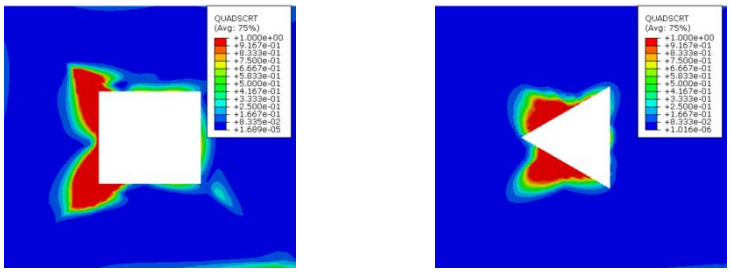
4.2.2 Effect of Delamination Shape

Using the circular prefabricated delamination with a diameter of 12 mm located at one-third of the laminate thickness (between plies 8 and 9) as the baseline, four different shapes, namely circular, elliptical, square, and triangular, were selected to introduce prefabricated delamination to analyze the effect of delamination shape on the joint structure.

The delamination propagation under different delamination shapes is shown in Fig. 4.10. For all shapes, delamination propagates outward along the compression side of the hole edge, with almost no propagation on the opposite side. The direction of damage propagation is mainly concentrated in the ±45° directions, because the prefabricated delamination is located between the 8th ply (-45°) and the 9th ply (45°), indicating that the propagation direction of the cohesive elements is correlated with the orientations of the adjacent plies. The delamination propagation is most severe under the square prefabricated delamination, followed by the triangular shape, while the elliptical shape exhibits the smallest propagation range.



(a) Circular prefabricated delamination (b) Elliptical prefabricated delamination



(c) Square prefabricated delamination (d) Triangular prefabricated delamination

Fig. 4.10 Delamination propagation for different delamination shapes

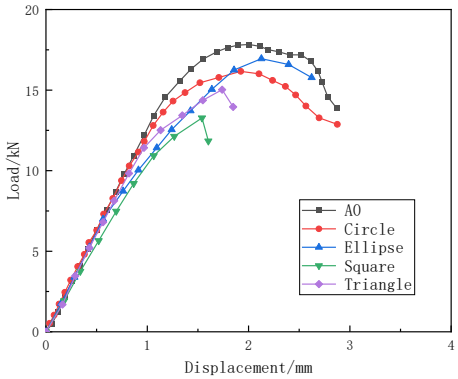


Fig. 4.11 Comparison of load-displacement curves obtained from finite element simulations for different delamination shapes

The load-displacement curves for different delamination shapes are shown in Fig. 4.11, where A0 represents the intact specimen. The curves show good consistency in the initial linear stage, indicating that the change in delamination shape has little effect on the overall stiffness of the structure. Different delamination shapes affect the ductility of the structure. The ductility under the square prefabricated delamination is the smallest, followed by the triangular shape, while the elliptical and circular shapes exhibit similar ductility. The comparison of ultimate load-bearing capacity under different delamination shapes is shown in Fig. 4.12. The intact specimen A0 has the largest ultimate load and the highest load-bearing capacity. The other four specimens with prefabricated delamination all show a certain degree of reduction in ultimate load-bearing capacity. Among them, the square prefabricated delamination results in the smallest ultimate load and the lowest load-bearing capacity.

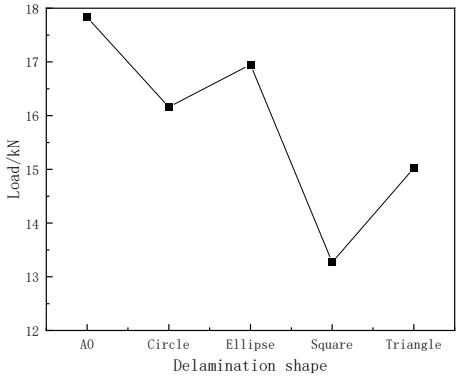
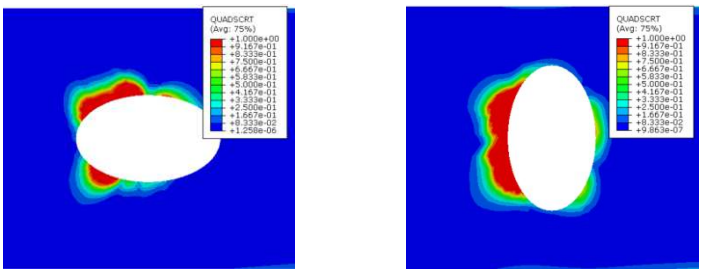


Fig. 4.12 Comparison of ultimate load-bearing capacity for different delamination shapes

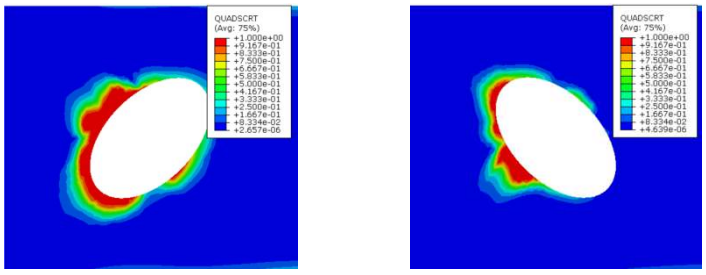
4.2.3 Effect of Delamination Orientation

Using the elliptical prefabricated delamination as the baseline, four orientations of 0°, 45°, -45°, and 90° were selected to introduce prefabricated delamination to analyze the effect of delamination orientation on the joint structure.

The delamination propagation under different delamination orientations is shown in Fig. 4.13. Delamination propagates outward along the compression side of the hole edge in all cases, with larger damage propagation ranges under the 90° and 45° prefabricated delamination conditions.



(a) 0° prefabricated delamination (b) 90° prefabricated delamination



(c) 45° prefabricated delamination (d) -45° prefabricated delamination

Fig. 4.13 Delamination propagation for different delamination orientations

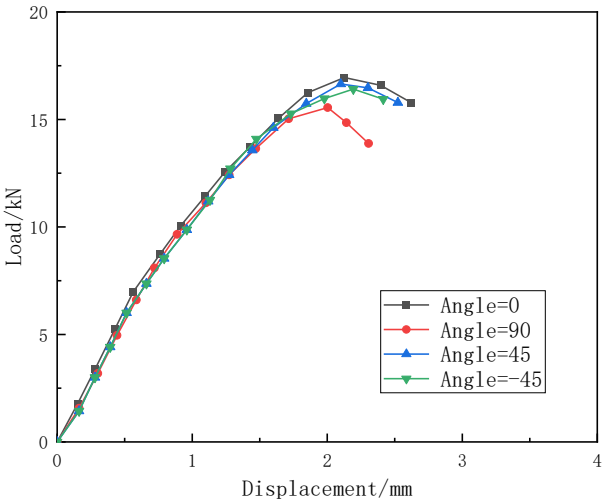


Fig. 4.14 Comparison of load-displacement curves obtained from finite element simulations for different delamination orientations

The load-displacement curves for different delamination orientations are shown in Fig. 4.14. The curves show good consistency in the initial linear stage, indicating that the change in delamination orientation has little effect on the overall stiffness of the structure. The comparison of ultimate load-bearing capacity under different delamination orientations is shown in Fig. 4.15. When the delamination orientation is 0°, the ultimate load is the largest and the load-bearing capacity is the highest. Under other orientations, the load-bearing capacity decreases to a certain extent. When the delamination orientation is 90°, the ultimate load decreases the most and the load-bearing capacity is the lowest.

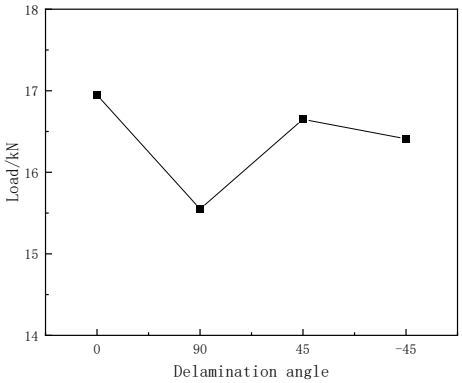


Fig. 4.15 Comparison of ultimate load-bearing capacity for different delamination orientations

4.3 Effects of Design Parameters on Static Strength of Single-Bolt Double-Shear Joints

Based on the finite element model established in this study, the effects of design parameters on the static strength of the single-bolt double-shear joint were further investigated to provide reference for the design and manufacturing of such joint structures.

4.3.1 Effect of Bolt Preload on Static Strength

In the composite single-bolt double-shear joint, the bolt is the key component connecting the metallic fixture and the composite laminate, and the application of bolt preload is involved during assembly. Different magnitudes of preload may affect the joint strength. To investigate this effect, different preload values were applied in the finite element model. The preload was calculated according to Eq. (4.1), and the specific values are listed in Table 4.4 (the values in parentheses are the corresponding tightening torques). The preload of 4250 N (Group 4) is the actual value applied to the test specimens in Chapter 2, and the other four groups serve as reference cases.

Table 4.4 Bolt preload values

Number	**Preload/N**
1	2500(2N.m)
2	3000(2.4N.m)
3	3500(2.8N.m)
4	4250(3.4N.m)
5	5000(4N.m)

The load-displacement curves obtained from finite element simulations under five different preload levels are shown in Fig. 4.16. The slopes of the initial linear stage differ under different preload levels. As the preload increases, the slope of the curve increases, indicating an increase in structural stiffness. In addition, the ultimate load also increases with increasing preload, indicating that a higher preload improves the load-bearing performance of the joint. This is mainly because the preload applies a lateral constraint to the laminate, which suppresses delamination propagation to a certain extent and thus enhances the load-bearing capacity. Therefore, in practical engineering applications, an appropriate increase in bolt preload can improve the load-bearing capacity of the joint. However, it should be noted that the preload should not be excessively large, as excessive preload may damage the surface structure of the laminate and the fixture, which would instead reduce the load-bearing performance.

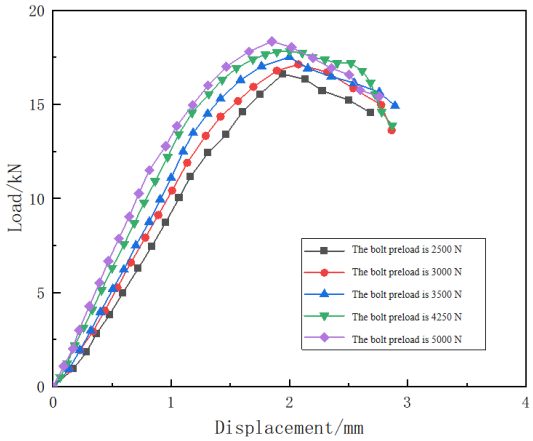


Fig. 4.16 Load-displacement curves of the joint structure under different bolt preloads

4.3.2 Effect of Bolt-Hole Clearance on Static Strength

During the manufacturing process of composite joint structures, the clearance between the bolt and the hole in the laminate is often present due to manufacturing tolerances. Changes in clearance may affect the strength performance of the joint structure. To investigate this effect, the finite element model established in this study was used. In the model, the hole diameter in the laminate is 4 mm. To vary the bolt-hole clearance, the laminate hole diameter was kept constant while the bolt shank diameter was varied. Five clearance levels of -1%, 0, 1%, 2%, and 4% were considered, where negative values correspond to interference fit and positive values correspond to clearance fit, as listed in Table 4.5.

Table 4.5 Bolt-hole clearances between the bolt and the laminate hole

No.	Boltshankdiameter/mm	Clearance	Fittype
1	4.04	-1%	Interference fit
2	4	0	
3	3.96	1%	Clearance fit
4	3.92	2%	Clearance fit
5	3.84	4%	Clearance fit

The load-displacement curves obtained from finite element simulations under five different clearance levels are shown in Fig. 4.17. The slopes of the initial linear stage are significantly different under different clearance levels. As the clearance increases, the slope decreases noticeably. When the clearance is 4%, the reduction in stiffness is particularly severe, indicating that the change in bolt-hole clearance affects the stiffness of the joint, mainly because the contact area between the bolt and the hole decreases under clearance fit conditions. In addition, as the clearance increases, the ultimate load decreases. Under interference fit (clearance of -1%), the ultimate load-bearing capacity of the structure is the largest. Under clearance fit (positive clearance values), a larger clearance leads to a smaller ultimate load-bearing capacity. This is because as the clearance increases, the contact between the bolt and the hole is delayed, which changes the contact state and causes the hole region to bear higher compressive stress under the same load, thereby reducing the overall strength of the structure. It can be concluded that interference fit increases the joint strength to a certain extent, while clearance fit significantly reduces the joint strength. In practical design and manufacturing, an appropriate interference fit can be considered for single-bolt double-shear joints.

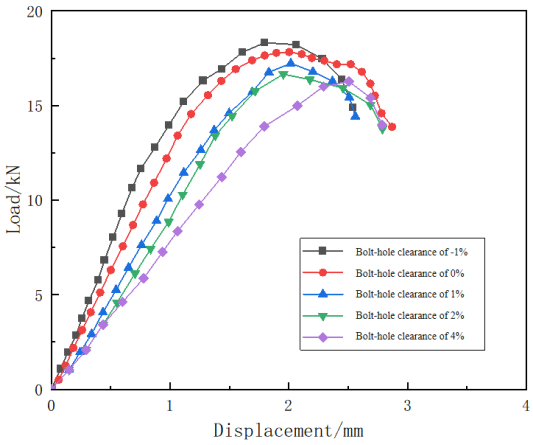


Fig. 4.17 Load-displacement curves of the joint structure under different bolt-hole clearances

4.3.3 Effect of Fixture Thickness on Static Strength

The metallic fixture is a key component of the composite single-bolt double-shear joint and plays an important role in the load-bearing performance of the structure. Different fixture thicknesses may affect the performance of the joint. To investigate this effect, finite element models with four different fixture thicknesses were established, as shown in Fig. 4.18. The thickness of 3 mm corresponds to the actual fixture used in the experiments in Chapter 2, while the thicknesses of 2 mm, 5 mm, and 8 mm serve as reference cases.

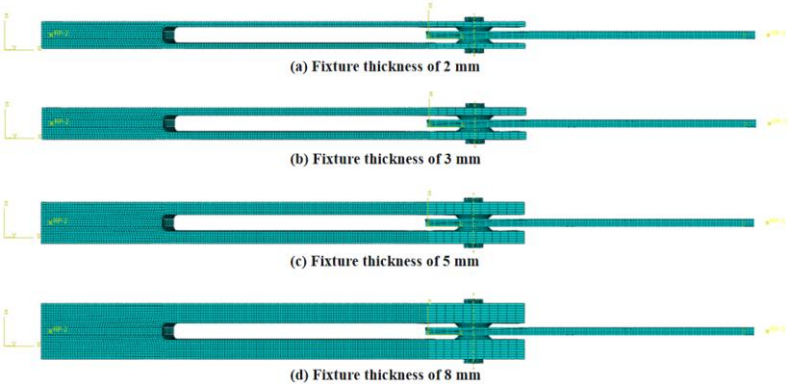


Fig. 4.18 Finite element models of the joint structure with different fixture thicknesses

The load-displacement curves obtained from finite element simulations under four different fixture thicknesses are shown in Fig. 4.19. The ultimate loads are relatively close under the four fixture thicknesses, indicating that the change in fixture thickness does not significantly affect the ultimate load-bearing capacity of the structure. However, the slopes of the initial linear stage differ under different fixture thicknesses, meaning that the stiffness of the structure is affected to a certain extent. As the fixture thickness increases, the structural stiffness increases. The stiffness is the smallest with a fixture thickness of 2 mm and the largest with a fixture thickness of 8 mm, while the stiffness with a thickness of 3 mm lies between the two. Therefore, in practical engineering applications, considering factors such as structural strength, stiffness, weight, and manufacturing cost, a fixture thickness of 3 mm is a reasonable choice for the metallic fixture of the composite single-bolt double-shear joint.

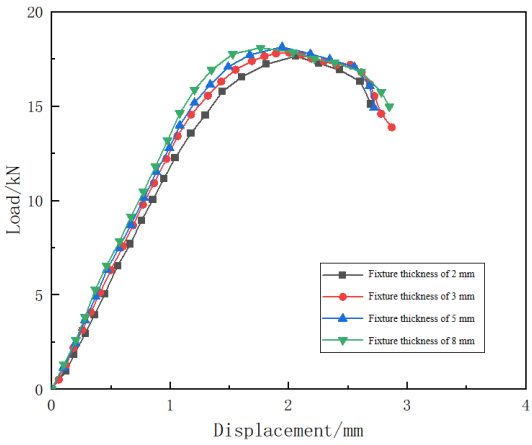


Fig. 4.19 Load-displacement curves of the joint structure under different fixture thicknesses

5.Conclusion

This paper presents a systematic experimental and numerical investigation on the tensile performance of composite single-bolt double-shear joints with prefabricated hole-edge delamination. A three-dimensional progressive damage model was developed and validated, and parametric analyses were conducted to examine the effects of delamination diameter, location, shape, and orientation on joint performance. Based on the experimental and numerical results, the following conclusions can be drawn:

(1) The proposed progressive damage model, incorporating the three-dimensional Hashin-type failure criterion and Camanho degradation model via a UMAT subroutine with zero-thickness cohesive elements for delamination simulation, accurately predicts the tensile response of composite single-bolt double-shear joints with prefabricated hole-edge delamination. The simulated ultimate loads agree well with experimental results, with relative errors within 10% across all delamination diameters (0 mm, 12 mm, 20 mm, and 28 mm). The load–displacement curves, failure modes, and delamination propagation patterns also show good consistency with experimental observations, validating the effectiveness of the numerical approach.

(2) Prefabricated hole-edge delamination significantly reduces the load-bearing capacity of the joint structure. As the delamination diameter increases from 0 mm to 28 mm, the average ultimate load decreases from 16.44 kN to 15.51 kN, a reduction of 5.7%. The failure modes are characterized by a combination of bearing failure, fibre breakage and buckling, matrix crushing and cracking, interlaminar delamination, and fiber-matrix shearing failure, which interact and couple with each other to accelerate structural failure.

(3) Delamination location, shape, and orientation all have pronounced effects on joint performance. Delamination near the mid-thickness of the laminate propagates more extensively due to weaker lateral constraint from bolt preload, resulting in greater reduction of load-bearing capacity. Among the four shapes examined, the square-shaped delamination causes the most

severe reduction in ultimate load (6.2% decrease compared with the intact specimen), while the elliptical shape exhibits the least detrimental effect (3.5% decrease), attributed to varying degrees of stress concentration from geometric discontinuities. The 90° delamination orientation leads to the greatest reduction in load-bearing capacity (5.4% decrease), while the 0° orientation causes the least reduction (3.1% decrease), as the 90° orientation aligns with the opening-mode stress component at the delamination front, which is more effective in driving propagation.

(4) A competitive mechanism governs delamination propagation: for small prefabricated delaminations (12 mm), propagation beyond the prefabricated region dominates the failure process; for large prefabricated delaminations (28 mm), coverage of the existing defect area predominates, with limited additional propagation. This indicates the existence of a critical delamination size below which failure is governed by propagation behavior and above which failure is governed by the prefabricated defect itself.

(5) Parametric studies on design factors reveal that increasing bolt preload enhances joint stiffness and ultimate load-bearing capacity by providing lateral constraint that suppresses delamination; interference fit improves joint strength while clearance fit reduces it; and fixture thickness primarily affects structural stiffness rather than ultimate strength.

6.Statements and Declarations

Funding:

This work was supported by the Aviation Science Foundation of China (Grant No. 2024M074052003).

Declarations:

Author Contributions:

Y.M. Li: Investigation, Formal analysis, Data curation, Visualization, Writing-original draft, Writing-review & editing.
Z.R. Wu: Conceptualization, Methodology, Project administration, Supervision, Funding acquisition, Writing-original draft, Writing-review & editing.
H. Lei: Resources, Validation.
S.Z. Ma: Investigation, Formal analysis, Visualization, Writing-review & editing.
W.Y. Yuan: Investigation, Formal analysis, Visualization, Writing- review & editing.
M.L. Chen: Investigation, Formal analysis, Data curation, Visualization.

Conflicts of Interest:

The authors declare that there are no conflicts of interest or competing interests.

Ethics Approval and Consent to Participate：

This study does not involve human participants or animals. Therefore, ethics approval is not applicable. And all authors have read and approved the final manuscript.

References

[1] Du SY, Guan ZD. Strategic considerations on advanced composite technologies for China's large passenger aircraft. Acta Materiae Compositae Sinica 2008;(1):1-10.

[2] Zhang X, Chen Y, Hu J. Recent advances in carbon fibre reinforced polymer composites for aerospace applications: a review. Composites Part B 2024;278:111438.

[3] Liu Y, Wang H, Li Z. High-performance composite materials in next-generation aircraft: a critical review. Progress in Aerospace Sciences 2025;145:101085.

[4] Li J, Sun Q, Zhao T. Advanced fibre-reinforced composites for lightweight aerospace structures: processing, properties and applications. Materials & Design 2023;233:112267.

[5] Li H, Zhang Y, Liu C. Composite applications in B787 and A350: a comparative study of structural design and performance. Aerospace Science and Technology 2024;146:108957.

[6] Yang Y. The path traversed: a chronicle of composite material development for China's C919 large passenger aircraft. China Science and Technology 2017;7:53-5.

[7] Xu Y. Performance analysis of carbon fiber composites and their application in aviation. Chemical Engineering & Equipment 2023;(5):200-2.

[8] Wang P, Chen X, Liu J. Sustainable lightweight design of composite aircraft structures: recent progress and future directions. Composite Structures 2024;336:118024.

[9] Camanho PP, Matthews FL. A progressive damage model for mechanically fastened joints in composite laminates. Journal of Composite Materials 1999;33(24):2248-80.

[10] McCarthy CT, McCarthy MA, Lawlor VP. Progressive damage analysis of multi-bolt composite joints with variable bolt-hole clearances. Composites Part B 2005;36(4):290-305.

[11] Duan YX. Study on preloading behaviour and static strength of interference-fit bolted joints in CFRP [Master's thesis]. Xi'an: Northwestern Polytechnical University; 2015.

[12] Green BG, Wisnom MR, Hallett SR. An experimental investigation into the tensile strength scaling of notched composites. Composites Part A 2007;38(3):867-78.

[13] Sols A, Sanchez-Saez S, Martinez X, et al. Numerical analysis of interlaminar stresses in open-hole laminates under compression. Composite Structures 2019;217:89-99.

[14] Zhang Y, Van Paepegem W, De Corte W. An enhanced progressive damage model for laminated fiber-reinforced composites using the 3D Hashin failure criterion: a multi-level analysis and validation. Materials 2024;17(21):5176.

[15] Liu YC, Lu J, Zhang HW, et al. Impact resistance optimization of composite laminates based on variable-fidelity surrogate model. Polymer Composites 2024;45(17):16075-96.

[16] Camanho PP, Matthews FL. A progressive damage model for mechanically fastened joints in composite laminates. Journal of Composite Materials 1999;33(24):2248-80.

[17] Zhang D, Zhou J, Wang J, et al. A comparative study on failure mechanisms of open-hole and filled-hole composite laminates: experiment and numerical simulation. Thin-Walled Structures 2024;200:111730.

[18] Kumar S, Singh KK, Ramkumar J. Effect of bolt preload on fatigue behaviour of composite single-lap joints under cyclic loading. Composite Structures 2025;329:118789.

[19] Khashaba U, Sebaey T, Alnefaie K. Failure and reliability analysis of pinned-joint composite laminates: effects of pin-hole clearance. Journal of Composite Materials 2012;47(18):2287-98.

[20] Liu L, Zhang J, Chen K, Wang H. Combined and interactive effects of interference fit and preloads on composite joints. 2014.

[21] Wang H, Li G, Zhang Z. Parametric study on bearing strength of composite bolted joints considering hole clearance and stacking sequence. Composites Part B 2026;310:112345.

[22] Khashaba UA. Delamination in drilling GFR-thermoset composites. Composite Structures 2004;63:313-27.

[23] Bolotin VV. Mechanics of delaminations in laminate composite structures. Mechanics of Composite Materials 2001;37(5-6):367-80.

[24] Bradley WL, Corleto CR, Goetz DP. Fracture physics of delamination of composite materials. AFOSR-TR-88-0020. 1987.

[25] Zou Z, Reid SR, Li S, Soden PD. Mode separation of energy release rate for delamination in composite laminates using sub-laminates. International Journal of Solids and Structures 2001;38:2597-613.

[26] Yu W, Wang S, Shi Y, Ding X. A method for predicting failure behavior in composite countersunk bolt connections based on Hashin-Puck criterion. Journal of Aerospace Propulsion Technology 2025;4(6).

[27] Chen YL, Hwu C. Strength and progressive failure predictions of T-joint laminated composites using 3D continuum damage modeling. Fibers and Polymers 2025;26(3):975-82.

[28] Zhang Y, Song L, Lei J, et al. Multiscale compressive failure analysis of wrinkled laminates based on multiaxial damage model. Materials 2026;18(19):4503.

[29] Zhao Y, Zhou J, Liu X, et al. Hole-edge delamination effects on bearing capacity of composite bolted joints: experimental and numerical investigation. Composite Structures 2025;330:118826.

[30] Li XN, Wang YS, Zhou XF. Research status of numerical simulation methods for delamination damage in composite laminates. Acta Materiae Compositae Sinica 2021;38(4):1076-86.

[31] Dugdale DS. Yielding of steel sheets containing slits. Journal of the Mechanics and Physics of Solids 1960;8:100-4.

[32] Alfano G, Crisfield M. Finite element interface models for the delamination analysis of laminated composites: mechanical and computational issues. International Journal for Numerical Methods in Engineering 2001;77(2):111-70.

[33] Harper PW, Hallett SR. Cohesive zone length in numerical simulations of composite delamination. Engineering Fracture Mechanics 2008;75(16):4774-92.

[34] Ullah H, Harland AR, Lucas T, et al. Finite-element modelling of bending of CFRP laminates: multiple delaminations. Computational Materials Science 2012;52(1):147-56.

[35] Ullah H, Harland AR, Silberschmidt VV. Experimental and numerical analysis of damage in woven GFRP composites under large-deflection bending. Applied Composite Materials 2012;19(5):769-83.

[36] Hashin Z, Rotem A. A fatigue failure criterion for fiber reinforced materials. Journal of Composite Materials 1973;7(4):448-64.

[37] Puck A, Schurmann H. Failure analysis of FRP laminates by means of physically based phenomenological models. Composites Science and Technology 1998;58(7):1633-62.

[38] Kovács N, Maia MA, Rocha IBCM, et al. Physically recurrent neural networks for computational homogenization of composite materials with microscale debonding. European Journal of Mechanics - A/Solids 2025;112:105668.

[39] Nath D, Ankit, Neog DR, et al. Application of machine learning and deep learning in finite element analysis: a comprehensive review. Archives of Computational Methods in Engineering 2024;31(5):2945-84.

[40] Zitoune R, Collombet F. Numerical prediction of the thrust force responsible of delamination during the drilling of the long-fibre composite structures. Composites Part A 2007;38:858-66.

[41] Zheng Y, Guo C, Zhang S. Recent advances in drilling-induced delamination of composite materials: mechanisms, modelling and mitigation. Journal of Manufacturing Processes 2025;125:458-73.

[42] Ho-Cheng H, Dharan CKH. Delamination during drilling in composite laminates. Journal of Engineering for Industry 1990;112:236-9.

[43] Jain S, Yang DCH. Effects of feedrate and chisel edge on delamination in composites drilling. Journal of Engineering for Industry 1993;115:398-405.

[44] Liu B, Zhang L, Liu A, Guedes Soares C. Integrated design method of marine C/GFRP hat-stiffened panels towards ultimate strength optimisation. Ocean Engineering 2025;317:120052.

[45] Kumpati R, Skarka W, Skarka M, Brojan M. Enhanced optimization of composite laminates: multi-objective genetic algorithms with improved ply-stacking sequences. Materials 2024;17(4):887.

[46] Puck A, Schurmann H. Failure analysis of FRP laminates by means of physically based phen-omenological models[J]. Composites Science and Technology, 1998, 58(7): 1633-1662.

[47] Tsai S W, Wu E M. A General Theory of Strength for Anisotropic Materials[J]. Journal of Composite Materials, 1971, 5(1): 58-80.

[48] Hashin Z, Rotem A. A Fatigue Failure Criterion for Fiber Reinforced Materials[J]. Journal of Composite Materials, 1973, 7(4): 448-464.

[49] Tserpes K I, Papanikos P, Labeas G，et. Fatigue damage accumulation and residual strength assessment of CFRP laminates[J]. Composite Structures, 2004, 63(2): 219-230.

[50] Sc T. A progressive failure model for composite laminates containing openings: Tan, S.C. Journal of Composite Materials Vol 25 No 5 (1991) pp 556-577[J]. Composites, 1991, 22(6): 474.

[51] Chang F K,Chang K Y. A progressive damage model for laminated composite containing s-tress concentration[J]. Journal of Composite Materials, 1987, 21(9): 834-855.

[52] Mccarthy C T, Mccarthy M A, Lawlor V P. Progressive damage analysis of multi-bolt composite joints with variable bolt–hole clearances[J]. Composites Part B, 2005, 36(4): 290-305.

[53] Tserpes K I, Labeas G, Papanikos P, et al. Strength prediction of bolted joints in graphite/epoxy composite laminates[J]. Composites Part B Engineering, 2002, 33(7): 521-529.

[54] Zhao L, Gong Y, Zhang J, Chen Y and Fei B. Simulation of delamination growth in multidirectional laminates under mode I and mixed mode I/II loadings using cohesive elements[J]. Compos Struct. 2014, 116: 509-22.

[55] Chen J-F, Morozov EV and Shankar K. Simulating progressive failure of composite laminates including in-ply and delamination damage effects[J]. Composites Part A: Applied Science and Manufacturing. 2014, 61: 185-200.

[56] A.Hillerborg, M.Modeer, P.E.Petersson. Analysis of crack formation and crack growth in concrete by means of fracture mechanics and finite elements[J]. Cement and Concrete Research. 6(1976), 773-782.

[57] Harper PW, Hallett SR. Cohesive zone length in numerical simulations of composite delamination[J]. Eng Fract Mech 2008, 75(16):4774-92.

[58] Soden P D，Hinton M J，Kaddour A S．Lamina Properties，Lay up Configurations and Loading Conditions for a Range of Fibre- reinforced Composite Laminates[J]． Composites Science and Technology, 1998, 58(7):1011-1022．

Supplementary Files

This is a list of supplementary files associated with this preprint. Click to download.

- HighlightsV1.docx